Asymmetric Modulation of ENSO Teleconnections by the Interdecadal Pacific Oscillation

BO DONG,[a] AIGUO DAI, MATHIAS VUILLE, AND OLIVER ELISON TIMM

Department of Atmospheric and Environmental Sciences, University at Albany, State University of New York, Albany, New York

(Manuscript received 3 October 2017, in final form 25 April 2018)

ABSTRACT

Remote influences of ENSO are known to vary with different phases of the interdecadal Pacific oscillation (IPO). Here, observational and reanalysis data from 1920 to 2014 are analyzed to present a global synthesis of the IPO's modulation on ENSO teleconnections, followed by a modeling investigation. Regressions of surface air temperature T, precipitation P, and atmospheric circulations upon IPO and ENSO indices reveal substantial differences between ENSO and IPO teleconnections to regional T and P in terms of spatial pattern, magnitude, and seasonality. The IPO's modulation on ENSO teleconnections asymmetrically varies with both IPO and ENSO phases. For a given ENSO phase, IPO's modulations are not symmetric between its two phases; for a given IPO SST anomaly, its influence depends on whether it is superimposed on El Niño, La Niña, or neutral ENSO. The IPO modulations are linked to the atmospheric response to tropical SST anomalies, manifested in the local Hadley circulation and the local Walker circulation at low latitudes and the Rossby wave train in the extratropics, including the Pacific–North American (PNA) pattern in the Northern Hemisphere. A set of numerical experiments using CAM5 forced with different combinations of the IPO- and ENSO-related SSTs further shows that the asymmetric modulation arises from the nonlinear Clausius–Clapeyron relation, so that the atmospheric circulation response to the same IPO-induced SST departure is larger during a warm rather than a cold ENSO phase, and the response to a warm IPO state is larger than that to a cold IPO state. The asymmetry depends primarily on the tropical Pacific mean state and tropical SST anomalies and secondarily on extratropical SST anomalies.

1. Introduction

The interdecadal Pacific oscillation (IPO) is the leading mode of 40–60-yr variability in the Pacific sea surface temperatures (SSTs) (Zhang et al. 1997; Liu 2012). Through interactions with the atmosphere, the IPO affects temperature, precipitation, and other climate fields (referred to as teleconnection; e.g., Dong and Dai 2015, 2017) over other ocean basins (Dong et al. 2016) and many land regions, such as southern Africa, the Sahel, Australia, India, South America, and western North America (e.g., Power et al. 1999; Krishnan and Sugi 2003; Deser et al. 2004; Hartmann and Wendler 2005; Garreaud et al. 2009; Whitfield et al. 2010; Dai 2013; Dai et al. 2015; Dong and Dai 2015, 2017).

Since the IPO-related SST anomalies exhibit spatial patterns similar to those of El Niño–Southern Oscillation (ENSO), the IPO is naturally referred to as the ENSO-like interdecadal variability (Zhang et al. 1997). Whether the IPO is distinct from ENSO, either physically or statistically, has been debated in many studies (e.g., Dai 2013; Dong and Dai 2015; Westra et al. 2015; Newman et al. 2016), although we think there exist sufficient differences in their temporal and spatial characteristics to warrant a separation between the two. Nevertheless, because of their similar SST patterns, the IPO's teleconnections to regional climate may resemble those of ENSO on interannual time scales. Indeed, regions influenced by the IPO (Dai 2013; Dong and Dai 2015) generally follow those affected by ENSO (e.g., Ropelewski and Halpert 1987; Halpert and Ropelewski 1992; Dai and Wigley 2000; Trenberth et al. 2002; Chen et al. 2008; Newman et al. 2016). However, substantial differences are noticed between the impacts of the two modes. For example, increased winter precipitation over the

[a] Current affiliation: Department of Meteorology, University of Reading, Reading, United Kingdom.

Corresponding author: Dr. Aiguo Dai, adai@albany.edu

DOI: 10.1175/JCLI-D-17-0663.1

southeastern United States is observed during El Niño but not during the warm IPO phase, even though tropical Pacific SSTs are warmer than normal for both cases (Dai and Wigley 2000; Dong and Dai 2015). To better understand the Pacific SST's impacts on regional climate at ENSO and IPO time scales, here we work toward a quantitative global synthesis and comparison of ENSO's and IPO's teleconnections to regional climates.

Besides interdecadal covariations of surface temperature T and precipitation P over many regions with Pacific SSTs, ENSO's influences on regional climates are also found to vary with IPO phases. For example, Power et al. (1999) examined the year-to-year correlation between the Southern Oscillation index (SOI) and various climate variables in Australia including temperature, rainfall, river flow, and crop yield, and found that a robust ENSO–Australian climate interannual relationship only exists during cold phases but not during warm phases of the IPO. Similar modulation of the SOI–Australian precipitation relationship was further confirmed by Arblaster et al. (2002) in a coupled climate model and by Dong and Dai (2015) using longer observational records and different ENSO and IPO indices. Other than Australia, interdecadal modulation of ENSO–T or ENSO–P correlations by the IPO also exists over southern Africa and northern India, but not over western Canada and the southwestern United States, although the climates in all these regions are significantly influenced by both ENSO and IPO (Dong and Dai 2015).

Categorizing the Indian summer monsoon rainfall into each pair of ENSO and the Pacific decadal oscillation (PDO, which is the North Pacific expression of the IPO) phases, Krishnamurthy and Krishnamurthy (2014) found that drought conditions are significantly linked to El Niño during warm phases of the PDO (which is also the warm phase of the IPO), while wet monsoons are more closely coupled with La Niña during PDO cold phases. Apart from their findings, we notice that anomalous rainfall response to combined ENSO–IPO years is not simply the add-up of rainfall anomaly of ENSO and IPO years, respectively. In addition, for a given ENSO state (e.g., El Niño or La Niña), the amount of precipitation change in response to a superposition of warm IPO phase does not equal a superposition of cold IPO phase. Similar phenomena are also noted in Kwon et al. (2013) and in a few AGCM modeling studies (e.g., Chung et al. 2014; Frauen et al. 2014). Such nonlinear dependency of the strength of the ENSO teleconnections on IPO phases is referred to as the "asymmetric modulation of ENSO teleconnections by the IPO" in our study.

Aside from the nonlinear variation of the asynchronous ENSO–Indian monsoon coupling with the IPO, over East Asia, Chen et al. (2013) showed that the East Asian summer monsoon (EASM) following an El Niño event is much stronger during positive PDO phases than during negative PDO phases. Other than major monsoon regions, similar asymmetry in the IPO's modulation of ENSO's influence, though with varying strength, is found over the continental United States (Gershunov and Barnett 1998; Goodrich and Walker 2011), South America (da Silva et al. 2011), and Europe (Bice et al. 2012; López-Parages et al. 2015). These studies further imply that ENSO's teleconnection is asymmetric for not only IPO phases, but also ENSO phases, although explicit quantification of such asymmetry is still lacking.

The causes for the spatial heterogeneity of IPO's influence on ENSO teleconnections are not well understood. Many hypotheses have been proposed to explain the asymmetry of the modulation, including shifts in the position of the Walker circulation (Arblaster et al. 2002), and changes in the strength of the Hadley circulation (Krishnamurthy and Krishnamurthy 2014) and the western North Pacific low-level anticyclone (Chen et al. 2013). While these studies have provided useful information on this topic, they focused on certain regions, examined different time periods and seasons, and used different data and methods. As a result, a self-consistent picture of the processes underlying IPO's modulation of ENSO teleconnections over the globe is still needed. Here, with consistent data and analysis technique, we set to systematically quantify this asymmetric modulation by means of global composite difference maps of climate and atmospheric circulation fields. Furthermore, we attempt to explain the modulation processes by conducting a group of coherently designed atmospheric model experiments which have not yet been touched in previous studies.

The aim of this study is to present a global view of IPO's modulation on ENSO teleconnections, including its asymmetry with respect to the warm and cold phases of both ENSO and IPO, and more importantly to investigate the underlying physical mechanisms. Specifically, through a series of model experiments, we investigate whether the IPO's modulation effect is different for El Niño and La Niña, and whether the modulation effect differs when the same El Niño (or La Niña) occurs under a warm or cold IPO phase. This modeling investigation focuses on the role of the underlying SST patterns in the tropical and extratropical Pacific. A better understanding of such modulation mechanisms can benefit and improve ENSO index–based climate reconstruction and prediction.

2. Data, method, and model simulations

a. Datasets

HadISST, version 1, gridded monthly SST data from the Met Office (Rayner et al. 2003) were used to define the IPO and ENSO modes in this study. Monthly

precipitation data over the oceans since 1979 were from the GPCP version 2.2 (v2.2) product (Huffman et al. 2009). We derived monthly precipitation over land by merging the Global Precipitation Climatology Centre (GPCC; available online at ftp://ftp.dwd.de/pub/data/gpcc/html/fulldata_v7_doi_download.html) (Schneider et al. 2014) version 7 (v7) product from 1920 to 2010 and the GPCP v2.2 data from 2011 to 2014. We used the monthly surface air temperature data over land from 1920 to 2014 from the Climatic Research Unit Temperature, version 4 (CRUTEM4), dataset obtained from the Climatic Research Unit (available online at http://www.cru.uea.ac.uk/cru/data/temperature/) (Morice et al. 2012). As in Dong and Dai (2015), long-term monthly mean and linear trends in T and P data were removed prior to all calculations and analyses, which focus on the period from 1920 to 2014, as SST and other data before 1920 are sparse.

We used a century-long atmospheric reanalysis product, the ECMWF twentieth century reanalysis (ERA-20C; available online at http://apps.ecmwf.int/datasets/data/era20c-daily/levtype=sfc/type=an/) (Poli et al. 2013) to examine atmospheric circulations associated with the IPO and ENSO. The ERA-20C assimilates observations of SST, surface and sea level pressure, and marine surface winds on a spectral T159 global Gaussian grid (approximately 125 km horizontal grid spacing) with 91 vertical levels (up to 0.01 hPa), and covers the period from 1900 to 2010. Seasonal atmospheric circulation patterns associated with the North Atlantic Oscillation (Hurrell 1995) and the Pacific–North American pattern (Wallace and Gutzler 1981) in the ERA-20C generally agree with those in the Twentieth Century Reanalysis, JRA-55, and ERA-Interim as shown by Poli et al. (2016), who also showed that none of these circulation patterns show clear trends or abrupt changes during 1900–2010. We used the ERA-20C data from 1920 to 2010, which contains relatively abundant surface observations and is sufficiently long for extracting the IPO-related component from atmospheric circulation fields. We also repeated our analyses using the Twentieth Century Reanalysis, version 2c (v2c) (Compo et al. 2011), but since the results (not shown) are generally similar, we will only present figures based on the ERA-20C reanalysis in sections 4 and 5.

b. Decomposition of atmospheric overturning circulation

To investigate the linkage between the IPO and precipitation variability in the tropics and subtropics, we decomposed the large-scale overturning circulation into zonal and meridional components to represent the local Walker circulation and local Hadley circulation at individual locations. Physically, both zonal and meridional overturning circulation satisfy continuity independently, which ensures that the complete overturning circulation is equal to the sum of the two orthogonal components. Following the method of Schwendike et al. (2014), a velocity streamfunction vector $\boldsymbol{\psi}$ is defined as

$$\nabla_p \cdot \psi = -\nabla_p^2 \mu = \omega, \tag{1}$$

where μ is a potential function, and ω is the vertical pressure velocity. The divergent wind can be written in expression of the velocity streamfunction as

$$\mathbf{U}_{\text{div}} = (U_\lambda, U_\phi) = -\frac{\partial \psi}{\partial p} = -\left(\frac{\partial \psi_\lambda}{\partial p}, \frac{\partial \psi_\phi}{\partial p}\right), \tag{2}$$

where U_λ and U_ϕ are the zonal and meridional components of the divergent winds, and ψ_λ and ψ_ϕ are the zonal and meridional components of $\boldsymbol{\psi}$, respectively. The vertical pressure velocity can be partitioned into the components that are associated, respectively, with the zonal and meridional components of the divergent winds:

$$\omega_\lambda \cos\phi = \frac{1}{a}\frac{\partial \psi_\lambda}{\partial \lambda} = \frac{1}{a^2 \cos\phi}\frac{\partial^2 \mu}{\partial \lambda^2} \quad \text{and} \tag{3}$$

$$\omega_\phi \cos\phi = \frac{1}{a}\frac{\partial}{\partial \phi}(\psi_\phi \cos\phi) = \frac{1}{a^2}\frac{\partial}{\partial \phi}\left(\cos\phi \frac{\partial \mu}{\partial \phi}\right), \tag{4}$$

where a is the radius of Earth, ϕ is the latitude, and ω_λ and ω_ϕ are the vertical motion components resulting, respectively, from the zonal and meridional components of the divergent winds. The vertical mass fluxes (in $\text{kg m}^{-2}\,\text{s}^{-1}$) at a given location associated with the zonal and meridional circulation components are, respectively,

$$m_\lambda = \frac{-\omega_\lambda \cos\phi}{g} \quad \text{and} \tag{5}$$

$$m_\phi = \frac{-\omega_\phi \cos\phi}{g}, \tag{6}$$

where g is the gravitational constant. This orthogonal decomposition can attribute the large-scale circulation to zonal and meridional components at each location, although in the tropics and subtropics, it is more straightforward to link circulation changes to tropical convective heating anomalies.

c. Model experiments

A set of numerical experiments (Table 1) were conducted to investigate how the IPO modulates ENSO teleconnections. We employed the Community Atmosphere Model, version 5.1.1 (CAM5; Neale et al. 2010), which is coupled to a land model (CLM4.5; Oleson et al. 2013), a thermodynamic-only sea ice model (CICE 5.1;

TABLE 1. List of CAM5 experiments in this study. All were run for 55 years, with the average of the last 50 years being used.

Model expt	SST scheme
CTL	Control run with 1920–2014 mean monthly SSTs from HadISST.
El Niño	El Niño SST anomaly superimposed on CTL.
La Niña	La Niña SST anomaly superimposed on CTL.
IPO+	Positive-phase IPO SST anomaly superimposed on CTL.
IPO−	Negative-phase IPO SST anomaly superimposed on CTL.
IPO+/El Niño	Positive-phase IPO and El Niño SST anomaly superimposed on CTL.
IPO−/El Niño	Negative-phase IPO and El Niño SST anomaly superimposed on CTL.
IPO+/La Niña	Positive-phase IPO and La Niña SST anomaly superimposed on CTL.
IPO−/La Niña	Negative-phase IPO and La Niña SST anomaly superimposed on CTL.

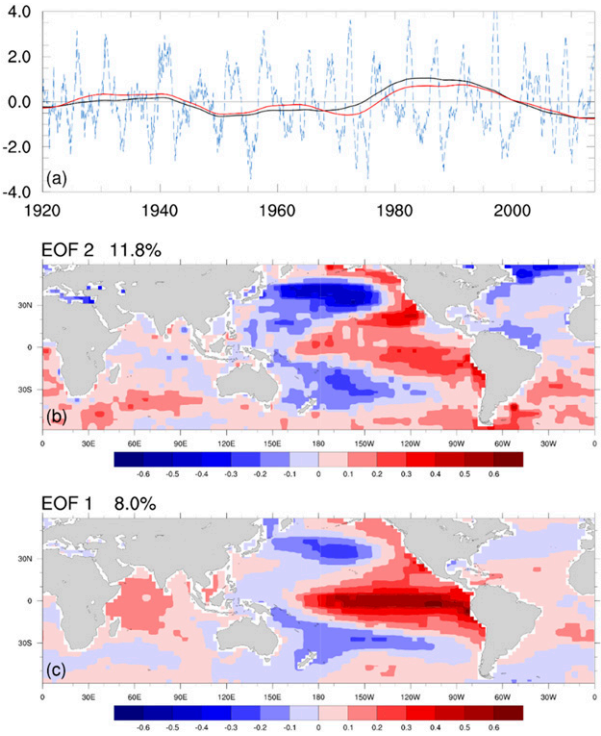

FIG. 1. (a) Smoothed second PC (black curve) of the 9-yr moving averaged annual SST and the leading PC (blue curve) of the high-passed (with the 9-yr moving average removed) monthly SST for 1920–2014 between 60°S and 60°N. The red curve is the IPO index in Dong and Dai (2015). (b) EOF pattern associated with the second PC [black curve in (a)], i.e., the IPO mode. (c) EOF pattern associated with the first PC [blue curve in (a)], i.e., the ENSO mode. The percentage variance explained by the EOF mode is shown on top of (b) and (c). The product of the PC and EOF coefficients is the SST anomaly (°C) represented by the EOF mode.

Hunke et al. 2015), and prescribed ocean surface boundary conditions (i.e., specified SSTs and sea ice). The CAM5 is the atmospheric component of the Community Earth System Model, version 1 (CESM1; Vertenstein et al. 2013). Both the CAM5 and CESM1 have been thoroughly evaluated and used widely in climate research (Hurrell et al. 2013). Particularly, precipitation patterns and variability across the globe have been documented to be satisfactorily simulated in different versions of CAM5 (Yuan et al. 2013; Li et al. 2015; Qian et al. 2015). Our own examinations showed that the CAM5 reproduces well the observed annual and seasonal T and P patterns in our control run and the composite ENSO-related T and P anomalies in our ENSO runs (Figs. A1–A4 in the appendix). The T response over land to IPO-related SST forcing also appears to be reasonable (Fig. A6), while the P response to IPO-related SST forcing seems to be weak in the model compared with the observations (Fig. A5), although oceanic precipitation observations are short.

We ran the CAM5 model at approximately 2° resolution, with prescribed monthly varying SSTs and sea ice derived from HadISST, and fixed solar irradiance, greenhouse gases (GHGs), and aerosols at year 2000. We first performed a control simulation (CTL) forced with 1920–2014 averaged monthly SSTs and sea ice concentrations from HadISST over the globe. It started from a previous control run and was integrated for 55 years, with the last 50 years being used as 50 realizations of the annual cycle. This case corresponds to the neutral ENSO and neutral IPO conditions in section 5, and serves as the baseline case for all other simulations. We then conducted a set of sensitivity experiments with ENSO-associated or/and IPO-associated SSTs to investigate how the IPO modulates the ENSO–T and ENSO–P relationship over different regions. We reconstructed the SST anomalies for an IPO positive phase (IPO+) as the product of the EOF-based (details in section 3) spatial SST pattern in Fig. 1b and one standard deviation (SD) of its principal component (PC) in Fig. 1a. The anomaly SST field was then multiplied by −1 to represent the SST anomalies for an IPO negative phase (IPO−). These time-invariant IPO-associated SST anomaly fields were added onto the CTL SST fields and then used as the boundary condition for CAM5 simulations of positive and negative phases of IPO, denoted as IPO+ and IPO− simulations, respectively.

Besides the IPO cases, the CAM5 was also run with SST fields associated with typical El Niño and La Niña, separately. Monthly El Niño– and La Niña–related SST anomalies were similarly generated as for the IPO but with an annual cycle, which is derived by averaging all December-centered annual ENSO cycles in the ENSO

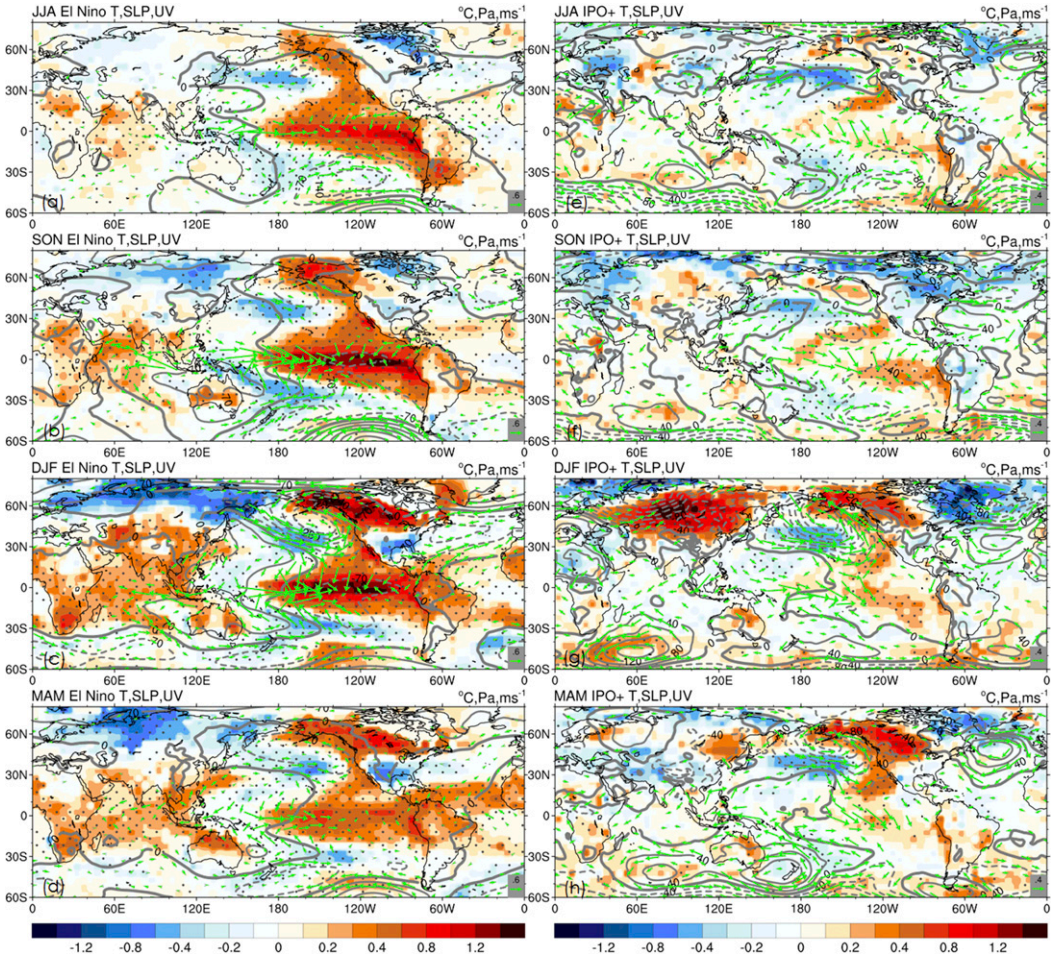

FIG. 2. Anomaly T (color shading; °C), SLP (contours; Pa), and surface wind (green vectors; m s^{-1}) associated with typical El Niño for (a) JJA, (b) SON, (c) DJF, (d) MAM, reconstructed from observations and ERA-20C based on linear regression described in section 4. (e)–(g) As in (a)–(d), but for IPO+. The T anomalies over dotted areas are statistically significant at the 10% level.

index in Fig. 1a. For the purpose of examining the linearity of the IPO's modulation on ENSO teleconnections, SST anomalies for La Niña are prescribed as the opposite to those for El Niño. Furthermore, with the idealized IPO and ENSO SST anomaly fields, we generated four combinations for ENSO and IPO being in phase (IPO+/El Niño and IPO−/La Niña), and out of phase (IPO−/El Niño and IPO+/La Niña) (see Figs. 11e–h). These combined SST anomaly fields were added to the CTL SST fields to produce the SST fields for the four additional CAM5 simulations. For each of the eight sensitivity cases, we ran 55 years, and the last 50 years of simulations were averaged to produce the results shown in section 6.

3. The IPO and ENSO patterns and indices

In this study, the IPO is defined as the second empirical orthogonal function (EOF) mode of 9-yr moving–average annual SST anomaly fields from 60°S to 60°N for 1920–2014 (Fig. 1b). The first EOF mode is a trend, essentially representing global warming. Our EOF-based IPO definition is consistent with previous studies (e.g., Parker et al. 2007; Dong and Dai 2015), although spatial patterns of the IPO mode differ slightly. We then applied another 9-yr moving averaging to the PC time series of the IPO mode to derive the IPO index (black curve in Fig. 1a). The IPO according to this index is characterized by two warm (or positive) phases from about 1924 to 1945 and from about 1977 to 1998, and two cold (or negative) phases from about 1946 to 1976 and from about 1999 to the present (2014). These phase periods are consistent with previous studies reviewed in the introduction (e.g., Zhang et al. 1997; Dong and Dai 2015). In addition, similar to Zhang et al. (1997), we performed an EOF analysis on the 9-yr high-pass-filtered (i.e., with the 9-yr average being removed)

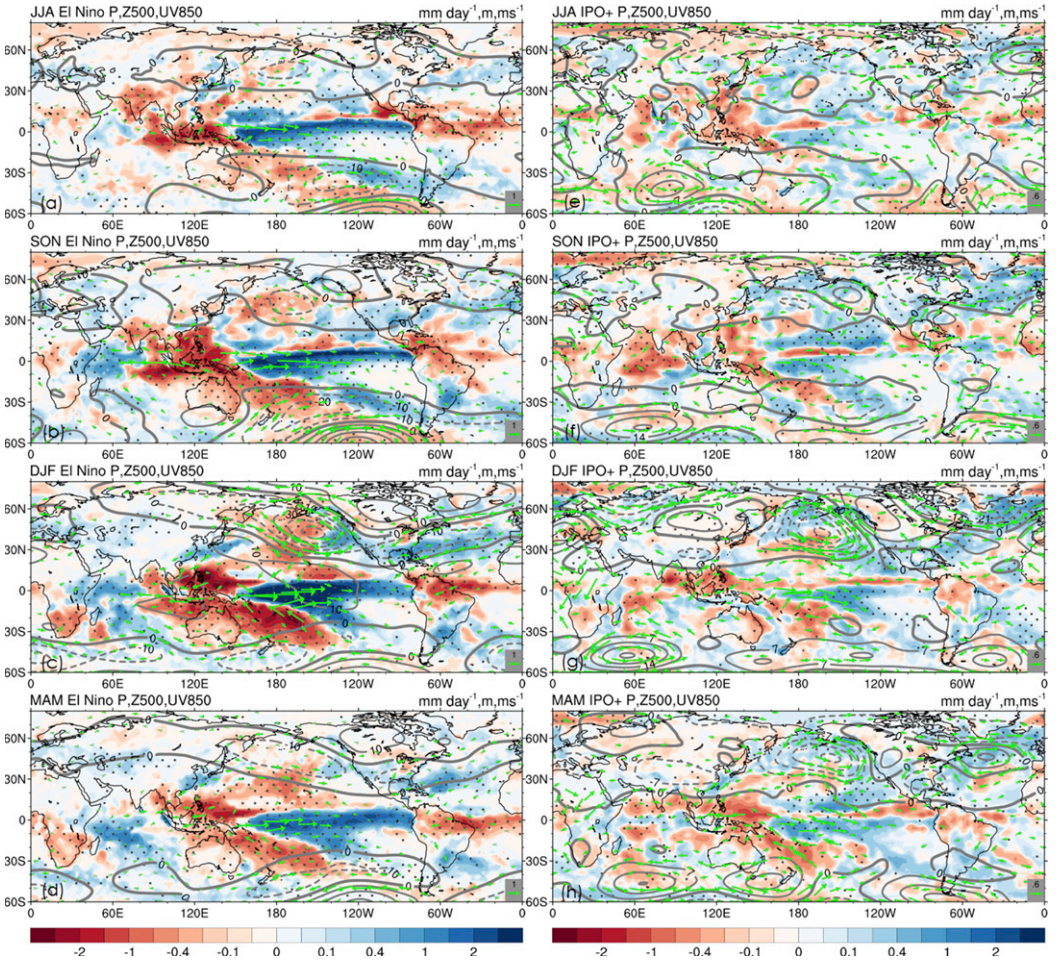

FIG. 3. As in Fig. 2, but for P (color shading; mm day^{-1}), geopotential height at 500 hPa (contours; m), and winds at 850 hPa (green vectors; m s^{-1}).

monthly SST fields from 60°S to 60°N and used the leading EOF mode to define ENSO (Fig. 1c), with the associated PC as the ENSO index (blue curve in Fig. 1a). Our IPO index (black line in Fig. 1a) is significantly correlated ($r = 0.92$) with the IPO index of Dong and Dai (2015) (red line in Fig. 1a), which was similarly derived except that the SST data were first 3-yr smoothed before the EOF analysis. The 9-yr smoothing of the SST data used here more effectively removes the interannual–multiyear variability associated with ENSO. This allows a separation of the EOF spatial patterns associated with the IPO and ENSO.

Figures 1b and 1c show that the SST anomaly patterns associated with the IPO are similar but not identical to those of ENSO. Specifically, the IPO-associated tropical SST anomalies extend farther poleward in the eastern Pacific than those for ENSO, and the IPO also has comparatively larger SST anomalies in the midlatitude North Pacific. In contrast, the ENSO-related SST variability is stronger in the equatorial Pacific. In low latitudes, unlike the conventional ENSO, whose largest variability extends from the eastern to central equatorial Pacific, the largest variability of the IPO is outside the equatorial Pacific (Fig. 1c). In addition, ENSO-related SST anomalies are larger over the Indian Ocean and South China Sea than those associated with IPO. Many of the differences in the spatial patterns for IPO and ENSO have been noted before (e.g., Zhang et al. 1997; Dong and Dai 2015).

The ENSO mode defined here represents the time-mean SST anomaly pattern averaged over all ENSO events, and the ENSO index is the spatially averaged mean evolution. Spatial SST patterns for individual El Niño and La Niña events may differ substantially. For example, the strongest anomaly can appear anywhere between the eastern (e.g., 1997/98 El Niño) and central tropical Pacific (e.g., 1991/92 El Niño), and the meridional extent also varies from one event to the next

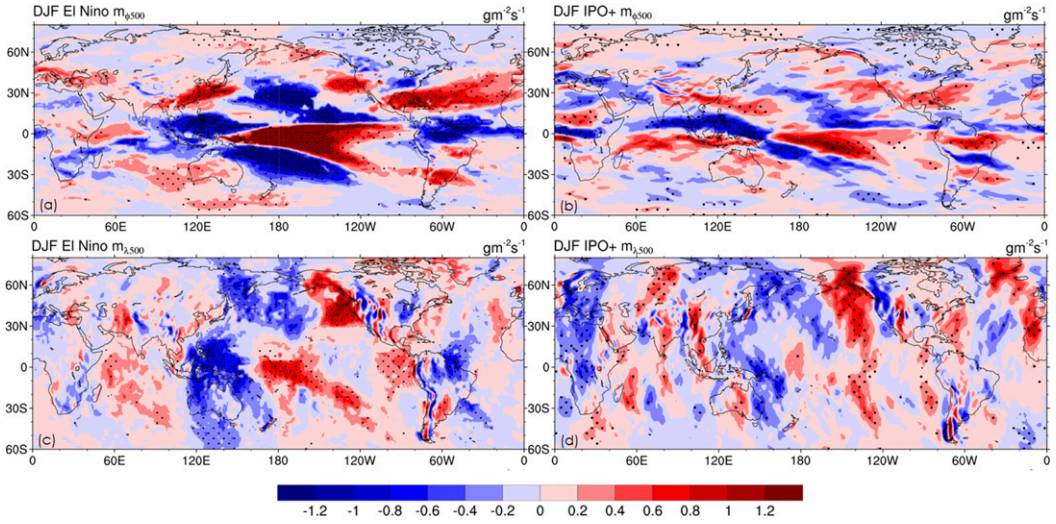

FIG. 4. Anomaly DJF 500-hPa (a),(b) m_ϕ (meridional) and (c),(d) m_λ (zonal) components of the vertical mass flux (g m^{-2} s^{-1}; positive for upward fluxes) associated with (left) El Niño and (right) IPO+ derived from the ERA-20C. Stippling indicates that the regression coefficient is statistically significant at the 10% level.

(Kug et al. 2009; Capotondi et al. 2015). The teleconnection analyses in this study are with respect to the canonical ENSO mode shown in Fig. 1c, and are for the purpose of quantifying interactions between the IPO and ENSO modes of different time scales.

4. Contrasting IPO's and ENSO's teleconnections

a. Comparison of IPO- and ENSO-related climate and circulation anomaly patterns

Surface temperature, precipitation, and atmospheric circulation anomalies associated with the IPO and ENSO are isolated through linear regression of these fields onto the IPO and ENSO indices, respectively. To obtain maximum covariance, the regression for ENSO was done similarly as in Chen et al. (2008), with up to 6 months of leads and lags. For the IPO mode, we calculated the regression with and without the ENSO-related anomalies and obtained similar results because of the weak correlation between the IPO and ENSO indices. We then reconstructed each of these anomaly fields as a product of the regression coefficient and one standard deviation of its corresponding index. As a result, Figs. 2–4 show "typical" teleconnection patterns for El Niño and a warm phase of the IPO. The anomaly

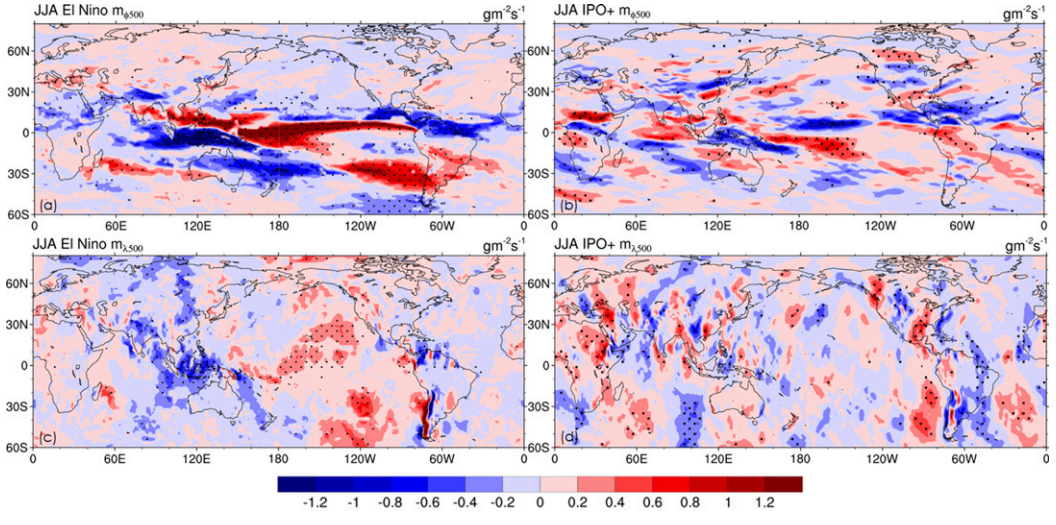

FIG. 5. As in Fig. 4, but for JJA.

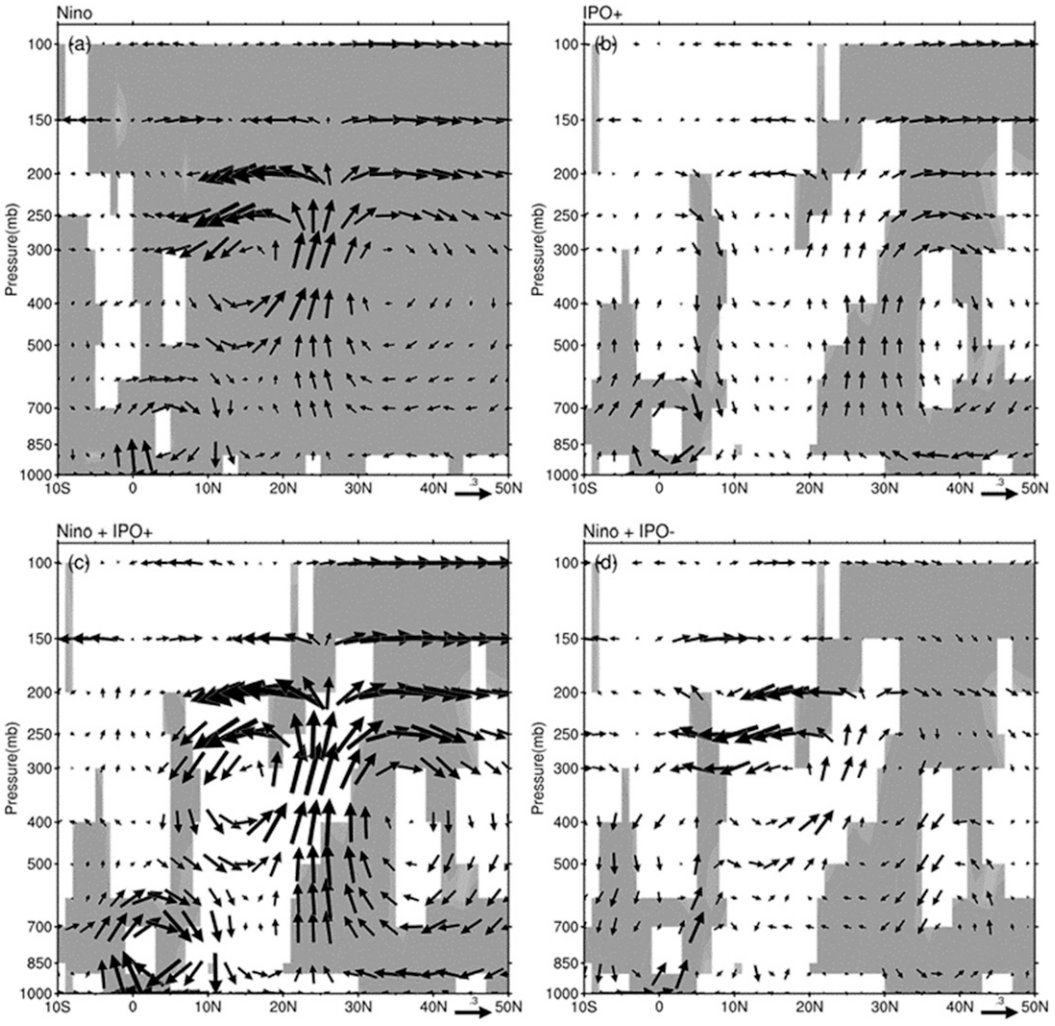

FIG. 6. Anomaly DJF 120°–60°W averaged meridional overturning circulation (vectors) for (a) El Niño and (b) IPO based on the ERA-20C, and (c) is (a) plus (b), and (d) is (a) minus (b). A scaling factor of −40 was applied to the zonal-mean meridional component of vertical pressure velocity ω_ϕ (hPa s^{-1}) for visualization of the circulation structure together with zonal-mean meridional divergent wind v_{div} (m s^{-1}). Gray shading indicates that the anomaly circulations are statistically significant at the 10% level.

patterns for La Niña and cold-phase IPO are just the inverse of Figs. 2–4 based on our regression. Although there exists some asymmetry between teleconnections for El Niño and La Niña events (i.e., teleconnections are not symmetrically opposite in sign in most regions; Hoerling et al. 1997), we designed the symmetric SST forcing pattern to study asymmetric response of the atmosphere.

Figures 2a–d shows a clear seasonal cycle in SST anomalies in the tropical Pacific, which peak in boreal winter (DJF; Fig. 2c). This also applies to remote T anomalies over land. The teleconnections and anomaly circulations generally agree with previous analyses (e.g., Halpert and Ropelewski 1992; Trenberth et al. 2002; Larkin and Harrison 2005; Chen et al. 2008), including the most notable Pacific–North American (PNA) wave train pattern (Wallace and Gutzler 1981), which is shown more clearly in the 500-hPa height field in Figs. 3b–d.

For IPO warm phases, tropical Pacific SST and surface trade wind anomalies (Figs. 2e–h) do not change with season as greatly as for the El Niño case. Over land, large surface air temperature anomalies appear only in DJF and MAM, when warmer conditions are seen over Eurasia, Alaska and western Canada, and northeastern Australia (Figs. 2e–h). They are similar to the annual patterns shown in Dong and Dai (2015). Together with a deeper Aleutian low and anomalous westerly winds in the North Pacific (Figs. 3g,h), T anomalies, mainly in the North Pacific and North America, are comparable to those of El Niño (Figs. 2c,d), although the tropical SST

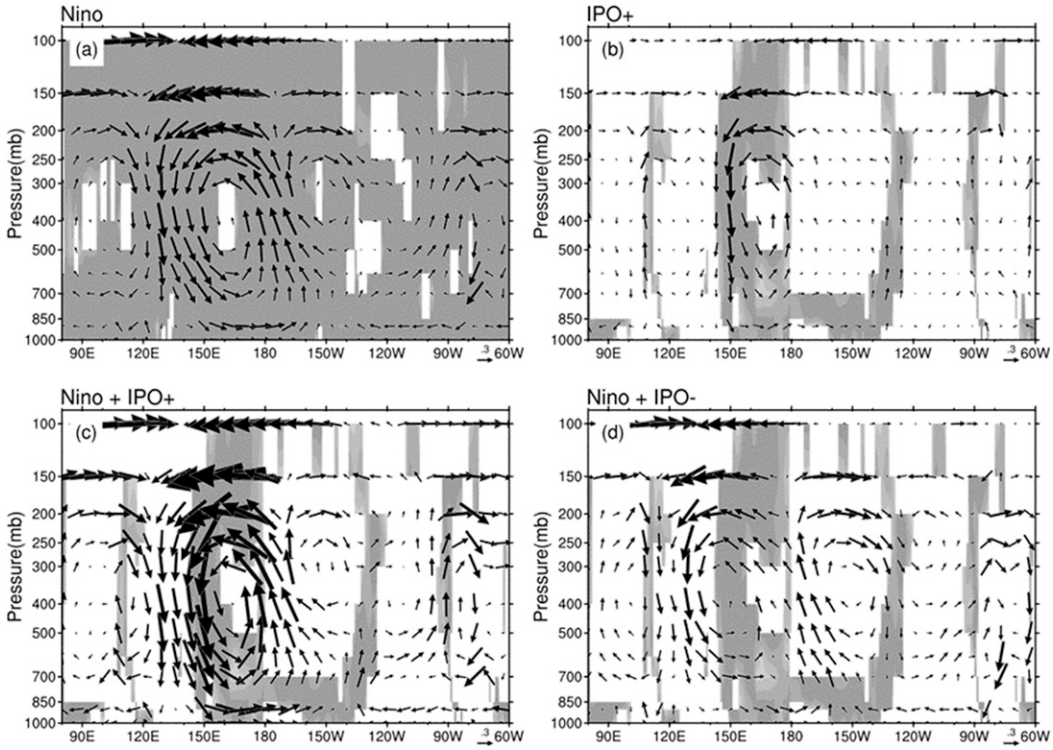

FIG. 7. Anomaly DJF 25°S–5°N averaged zonal overturning circulation (vectors) for (a) El Niño and (b) IPO based on the ERA-20C, and (c) is (a) plus (b), and (d) is (a) minus (b). A scaling factor of −90 was applied to the zonal component of vertical pressure velocity ω_λ (hPa s^{-1}) for visualization of the circulation structure together with the zonal divergent wind u_{div} (m s^{-1}). Gray shading indicates that the anomaly circulation is locally statistically significant at the 10% level.

forcing from the IPO is much smaller. The IPO-induced SST, *T*, and North Pacific circulation anomalies in MAM are comparable to those in DJF, in contrast to the weakening tendency from DJF to the following MAM for El Niño. In the southern high-latitude Pacific, we do not see a similar anomalous anticyclone as for El Niño, but an anticyclonic flow appears in the southern Indian Ocean around 60°E, southeast of which are anomalous westerlies associated with a low-pressure cyclonic circulation between 50° and 60°S (Fig. 2g).

In DJF, a strong warming pattern covers a larger area over northern China, Mongolia, and Siberia, accompanied by a low-pressure cyclonic circulation northwest of the warming center (Fig. 2c), which corresponds to a high-pressure center for the recent IPO cold phase since around 1999. The IPO-related *T* anomalies over Eurasia have been noticed previously (e.g., Dai et al. 2015) and the resulting cooling trend in DJF over Eurasia since the early 1990s has been investigated in a number of studies (e.g., Cohen et al. 2014; Luo et al. 2016a,b). The southwesterly (northeasterly) surface winds blowing from the Black Sea and Caspian Sea toward Siberia as part of the cyclonic (anticyclonic) anomaly circulation advect relatively warm (cold) air into the warming (cooling) center during the IPO warm (cold) phase. This helps explain the recent cooling over central Eurasia (Cohen et al. 2014; Luo et al. 2017a,b). Different from the El Niño mode, we notice cold temperature and low SLP anomalies over eastern coastal Canada, Greenland, and around 50°N of the North Atlantic, and anomalous anticyclonic flow to the south. These patterns look like a response to cold SSTs over the northern North Atlantic shown in Fig. 1b, which partly resembles the Atlantic multidecadal oscillation (AMO; Deser and Blackmon 1993; Alexander et al. 2014), whose phase change is linked to the recent winter cooling over Eurasia (Luo et al. 2017b). We examined the correlation between the IPO and the similarly smoothed AMO index from 1920 to 2014, and found a correlation coefficient of −0.42. This correlation is mostly a consequence of the strong anticorrelation ($r = -0.94$) during 1980–2014 when the IPO (AMO) index exhibits a downward (upward) trend. This indicates that the IPO and AMO may be related to each other and the patterns over the North Atlantic are likely also linked to the AMO. Although it is interesting to contrast the IPO's and AMO's global climate consequences, it is beyond the scope of this research and thus not discussed here.

TABLE 2. Number of ENSO and combined ENSO–IPO cases occurring during 1920–2014 and 1979–2014 in parentheses.

Event type	No. of events
El Niño	23 (9)
IPO+/El Niño	10 (4)
IPO−/El Niño	13 (5)
La Niña	27 (8)
IPO+/La Niña	11 (4)
IPO−/La Niña	16 (4)
Total ENSO	50 (17)
ENSO neutral	45 (19)

Similar to the seasonal cycle of temperature shown in Figs. 2a–d, for El Niño the strongest *P* and circulation signals appear in DJF (Figs. 3a–d), consistent with previous studies (e.g., Ropelewski and Halpert 1987; Dai and Wigley 2000; Larkin and Harrison 2005). Precipitation patterns in DJF and MAM for warm IPO phases (Figs. 3g,h) resemble those of El Niño (Figs. 2g,h) to some degree, with a spatial correlation of 0.34 and 0.39, respectively. This broad spatial similarity does not exist for JJA and SON, when the circulation response is very weak for the IPO (Figs. 3e,f). Here we focus on contrasting DJF teleconnection patterns for the two modes. A wet rainfall band over the Pacific ITCZ and SPCZ and a dry band covering the Bay of Bengal, the northern Maritime Continent, and the Philippine Sea appear to be robust for the warm-phase IPO, but they are weaker than those for El Niño. In contrast to the El Niño case (Fig. 3c), the Pacific enhanced rainfall band of the warm-phase IPO (Fig. 3g) is shifted southward and accompanied by a narrow dry strip to the north of it along the equator. Easterly wind anomalies at 850 hPa are consistent with this dry strip. Wet anomalies over the southwestern United States and Mexico are comparable to those of El Niño (Figs. 3c,g). Over the North Pacific, associated with an anomalous cyclonic flow, there is also a dry–wet dipole pattern similar to that for El Niño (Figs. 3c,g), but with weaker amplitude and southward displacement. In SON and MAM, rainfall anomaly patterns over tropical and subtropical oceans are generally similar to those for DJF, but the anomalies are statistically insignificant over land.

b. *Overturning circulation anomaly patterns*

To help understand the rainfall anomaly pattern, we decomposed three-dimensional circulation into local

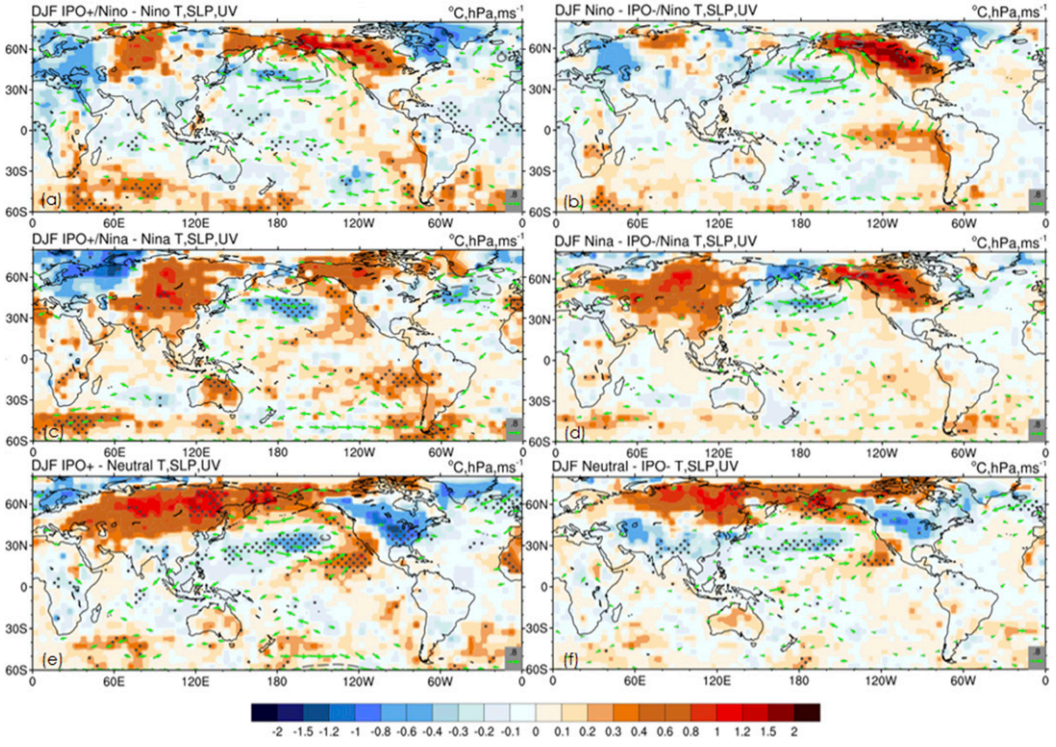

FIG. 8. Difference maps of DJF *T* (color shading; °C), SLP (contours; hPa), and surface winds (vectors; m s^{-1}) between (a) IPO+/El Niño and El Niño, (b) El Niño and IPO−/El Niño, (c) IPO+/La Niña and La Niña, (d) La Niña and IPO−/La Niña, (e) IPO+ and neutral ENSO, and (f) neutral ENSO and IPO−. Stippling indicates *T* changes are statistically significant at the 10% level.

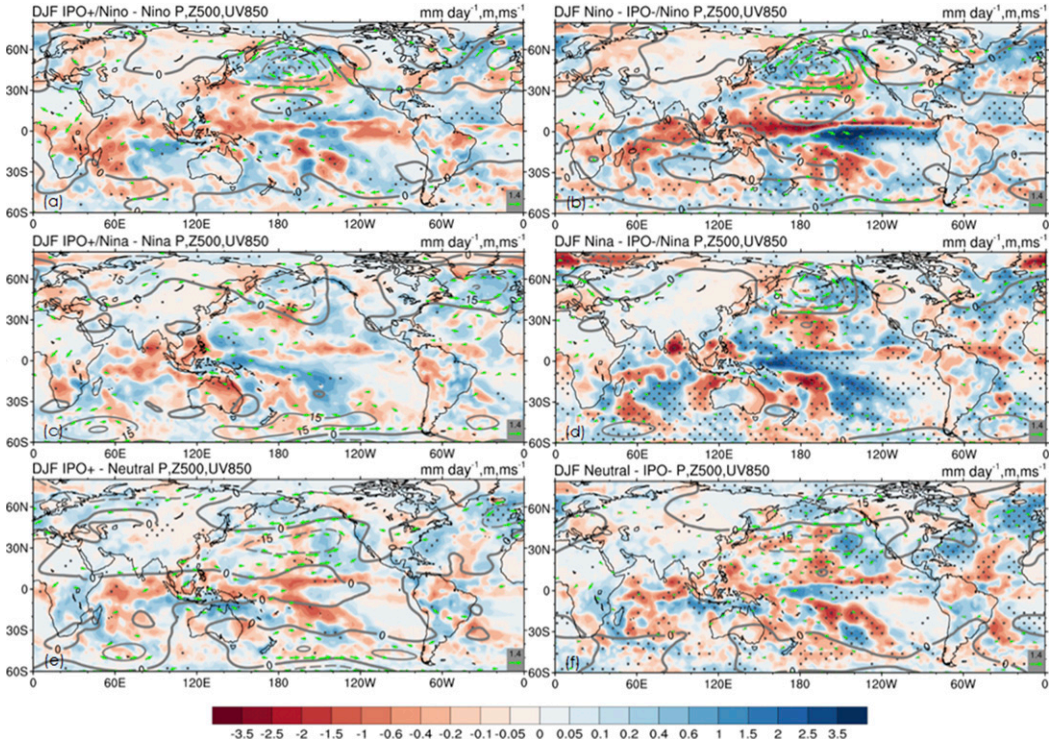

FIG. 9. As in Fig. 8, but for P (color shading; mm day^{-1}), geopotential height at 500 hPa (contours; m), and winds at 850 hPa (vectors; m s^{-1}).

zonal and meridional overturning circulations that link the SST and P anomalies associated with El Niño and warm phases of the IPO, and they are shown in Fig. 4 for DJF and Fig. 5 for JJA. In general, the meridional overturning circulations are stronger than the zonal overturning circulations, and the former broadly resembles the corresponding P anomaly patterns (Figs. 3a,c,e,g) in the tropics and subtropics. During El Niño boreal winter (Fig. 4a), anomalous ascending (descending) mass fluxes correspond well with the major wet (dry) rainfall bands in Fig. 3. Such a mass flux–precipitation relationship is also found over relatively smaller-scale land areas, such as southern Africa, southern China, southern Japan, and southern Brazil, Uruguay, and eastern Argentina.

This type of linkage also applies to the IPO mode, but it becomes less clear over many remote land regions, possibly due to the much weaker SST forcing. During boreal winter of warm IPO phases, the most prominent anomalies are seen over the tropical–subtropical Indo-Pacific region (Fig. 4b), where the meridional overturning circulation weakens over the Indonesian sector, with reduced upward mass fluxes over the equator (centered along the 5°N band) and reduced downward fluxes over the subtropics roughly along 10°S and 20°N. In contrast, the circulation strengthens over the central Pacific, with increased equatorial upward mass fluxes and enhanced downward mass fluxes off the equatorial region (Fig. 4b). This pattern extends from the central Pacific all the way to the Atlantic. There is a third zonal band of increased upward mass fluxes stretching from the central North Pacific to the southern United States and the subtropical western North Atlantic (Fig. 4b). This mass flux anomaly is consistent with wet conditions over the southern United States during IPO warm phases (Fig. 3g).

By comparing the mass flux anomaly patterns for El Niño and warm-phase IPO (IPO+), we can identify regions where there are significant interactions between them. For example, in DJF, we found enhanced upward mass fluxes for both El Niño and IPO+ across the southwestern United States and the Gulf of Mexico, including the nearby regions such as Florida (Figs. 4a,b). This common structure implies that during IPO+, the El Niño–related ascending motion and the resultant P anomaly are strengthened by the background SST conditions associated with the warm-phase IPO, and vice versa. Such a modulation mechanism is further illustrated in Fig. 6. Figures 6a and 6b show a shallow anomaly overturning circulation from the equator to around 10°N, and a deep anomaly overturning circulation with ascending motion around 20°–30°N, while corresponding subsidence occurs around 5°N (mostly

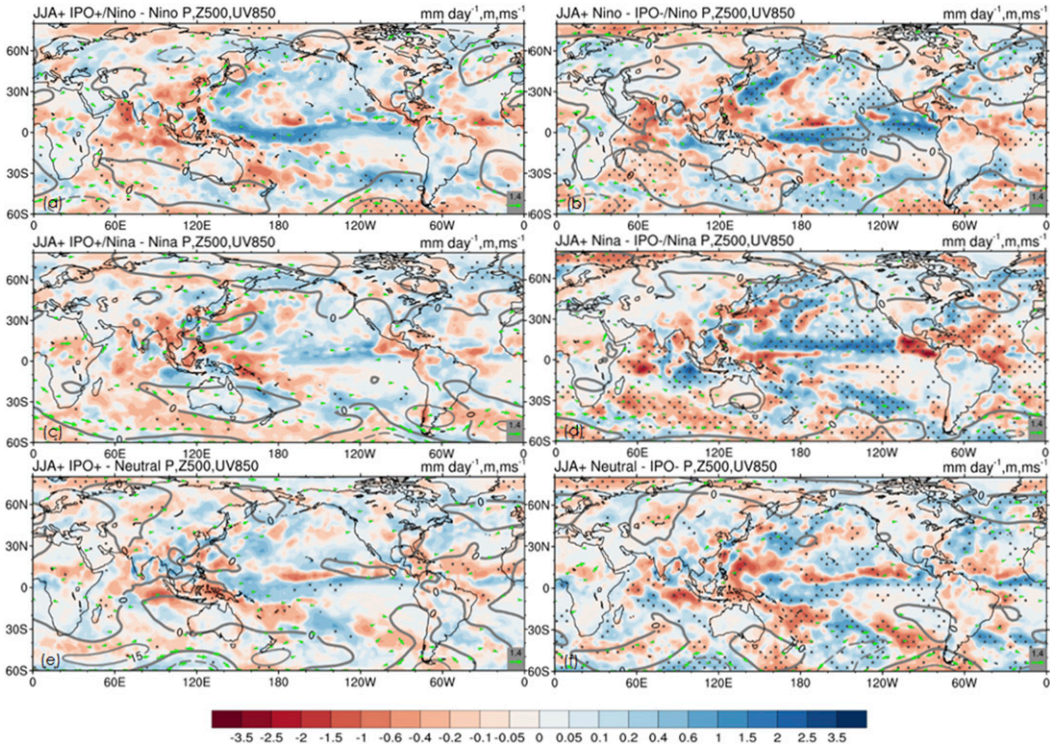

FIG. 10. As in Fig. 9, but for the JJA following an ENSO event.

in the upper-to-middle levels) and 40°–50°N. The combined anomaly circulation is amplified for the El Niño plus IPO+ case (Fig. 6c) but weakened considerably for the El Niño plus negative-phase IPO case (Fig. 6d).

For the zonal overturning circulation, the most noticeable departures during El Niño winter are prevailing descending mass fluxes over the western Pacific and the Maritime Continent, and ascending fluxes in the central tropical Pacific (Fig. 4c). For the warm IPO mode, this dipole flux pattern is displaced eastward and becomes weaker, with descending motion over the western Pacific and ascending motion in the central-eastern tropical Pacific, especially between 100° and 120°W (Fig. 4d). Both cases indicate an apparent weakening and eastward shift of the Walker circulation. The interaction of these two modes is further illustrated in Fig. 7. During IPO+, enhanced subsidence around 150°E and enhanced ascending motion around the date line occur during El Niño boreal winter (Fig. 7c). Opposite changes are shown in Fig. 7d for the El Niño boreal winter during cold IPO periods. In the extratropics, a wave train of alternating positive–negative mass flux anomalies is seen over the central North Pacific, stretching northeastward to western North America for both El Niño and warm IPO cases (Figs. 4c,d). This pattern resembles the positive PNA wave train, and the ascending (descending) locations are consistent with the low (high) pressure centers of the PNA (Figs. 2c,g) and positive (negative) *P* anomalies (Figs. 3c,g).

Although the magnitude of change in the local meridional overturning circulation (Fig. 4a, b) is generally larger than that in the local zonal overturning circulation (Figs. 4c,d), over some regions, changes in the local zonal circulation can dominate the total overturning circulation anomalies. For example, over eastern Australia, significant descending anomalies are seen during warm IPO boreal winter (Fig. 4d), which is mostly manifested as the western branch of the weakened Walker circulation (Fig. 7b) despite being partly offset by the ascending local meridional circulation anomaly (Fig. 4b). Such an anomaly circulation pattern is responsible for, on the one hand, the reduced summer precipitation over eastern Australia (Fig. 3g) during the warm IPO phase since anomalous descending motion suppresses convection. On the other hand, the weakening and eastward shift of the Walker circulation modifies the coupling of ENSO and Australia rainfall (Fig. 7): when El Niño (La Niña) takes place, the corresponding descending (ascending) anomaly is strengthened by the background descending (ascending) motion associated with IPO+ (IPO−), and therefore the coupling strength is enhanced.

In El Niño developing boreal summer, the anomaly overturning circulations (Fig. 5) are generally weaker

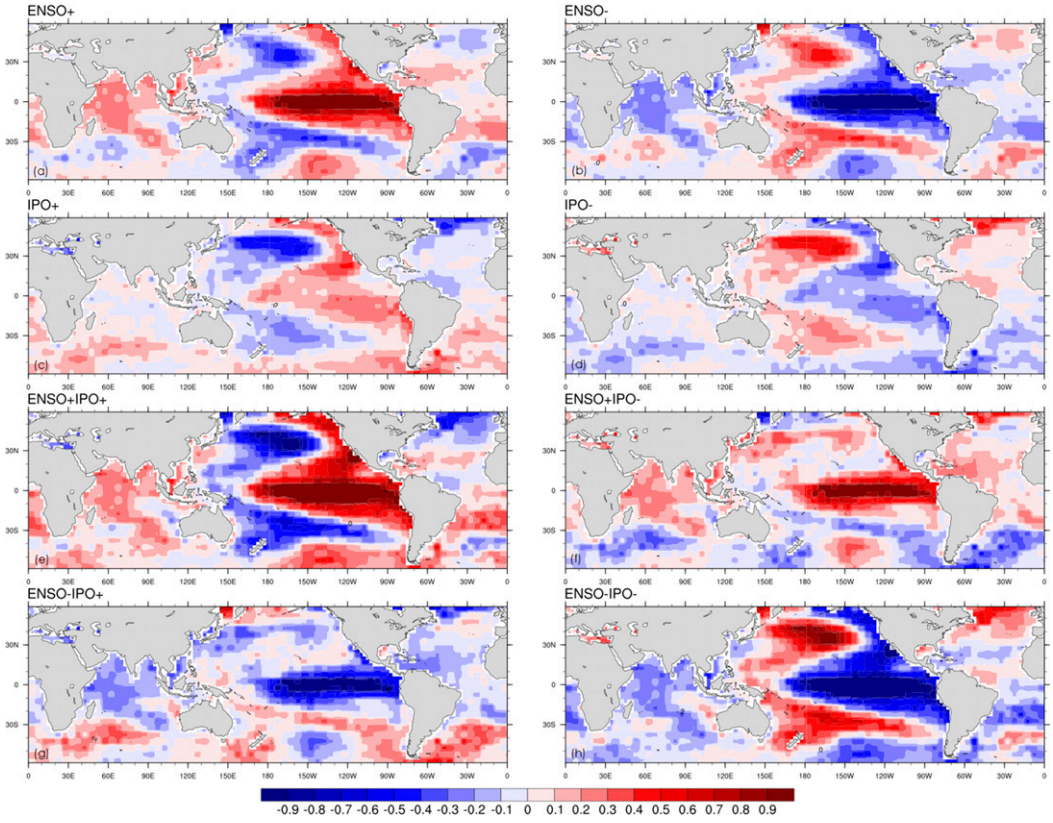

FIG. 11. Typical SST patterns for (a) El Niño, (b) La Niña, (c) IPO+, and (d) IPO−. The magnitude of the SSTs is determined as the product of the EOF (as in Fig. 1) and one SD of the associated PC. Composite SST patterns for (e) El Niño and IPO+, (f) El Niño and IPO−, (g) La Niña and IPO+, and (h) La Niña and IPO− are composed based on SSTs in (a)–(d).

than those in boreal winter (Fig. 4), especially for the zonal overturning circulation. Therefore, boreal summer rainfall anomalies largely result from changes in local meridional overturning circulation at most locations. For the El Niño case, an anomalous descending zone from the meridional component over northern India (Fig. 5a), together with a descending motion from the zonal component (Fig. 5c), works against the Indian summer monsoon circulation, leading to reduced monsoon rainfall there (Fig. 3a). During warm IPO phases, a regional overturning circulation anomaly is seen over northern China, characterized by anomalous rising motion around 25°N and sinking motion around 35°N (Fig. 5b). The direction of this circulation is opposite to the EASM mean circulation (Chen et al. 2013); consequently, the monsoon rainfall over northern China is reduced (Fig. 3e).

5. ENSO and IPO phase dependency of the IPO's modulation

In addition to Figs. 2e–h and 3e–h, we further examined IPO's modulation on ENSO teleconnections. In contrast to regional studies discussed in the introduction, we attempt to show the results in a different form, which aims to present a global picture showing where the largest modulation effects are located. Further, we investigate if the modulation is symmetric or asymmetric for IPO and ENSO phases. We first classified ENSO phases based on the monthly ENSO index in Fig. 1a. When the November–January (NDJ)-averaged ENSO index exceeds one standard deviation (SD) (below −1 SD), a typical El Niño (La Niña) event is identified. The ENSO events identified based on our criteria are consistent with those defined based on the oceanic Niño index (ONI; http://origin.cpc.ncep.noaa.gov/products/analysis_monitoring/ensostuff/ONI_v5.php). However, in contrast to the ONI and other ENSO indices, which include the low-frequency variations from the IPO, our ENSO mode and ENSO index exclude the IPO-related low-frequency variations and are uncorrelated with the IPO index, thus allowing us to separate their influences on T and P through linear regression. We then grouped these ENSO events into positive and negative IPO phases based on the IPO state of their

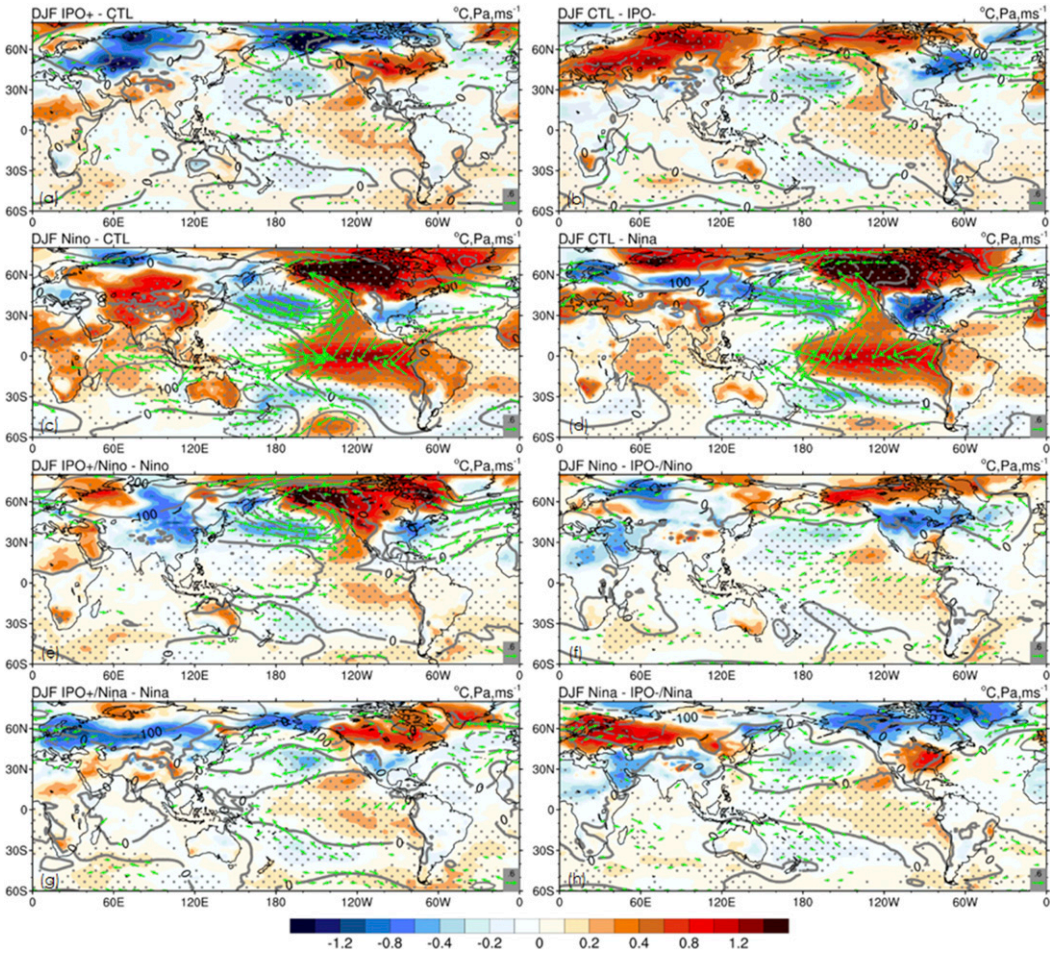

FIG. 12. Differences in CAM5-simulated DJF T (color shading; °C), SLP (contours; hPa), and surface winds (vectors; m s^{-1}) between (a) IPO+ and CTL, (b), CTL and IPO−, (c) El Niño and CTL, (d) CTL and La Niña, (e) IPO+/El Niño and El Niño, (f) El Niño and IPO−/El Niño, (g) IPO+/La Niña and La Niña, (h) La Niña and IPO−/La Niña. Stippling indicates that T changes are statistically significant at the 10% level

occurring time. This resulted in four categories: El Niño within a positive IPO phase (denoted as IPO+/El Niño), El Niño within a negative IPO phase (IPO−/El Niño), La Niña within a positive IPO phase (IPO+/La Niña), and La Niña within a negative IPO phase (IPO−/La Niña). The number of these cases occurring during 1920–2014 are listed in Table 2. Neutral ENSO cases (i.e., years without typical El Niño or La Niña events) are also analyzed here given that they occurred with a roughly equal chance as ENSO cases during the past century, although it represents more likely the IPO's stand-alone impact rather than its true modulation on ENSO.

Composites of T, P, and atmospheric circulation anomalies were generated for each of these six categories by averaging over the years for each case respectively, and also for all El Niño and all La Niña events. Prior to compositing, we counted the number of ENSO events that occurred during each period of IPO+ and IPO− separately and found that neither the frequency of El Niño and La Niña events nor their average strength vary with IPO phases, although the result may be sensitive to the choice of the ENSO index. The composite results are organized into two categories with El Niño and La Niña base state, respectively. For each ENSO state, whose T and P anomaly maps are already shown in Figs. 2 and 3, we present the IPO's net modulation effect using the difference map of the composite of all cases with relatively warm tropical Pacific SSTs minus the composite of all cases with relatively cool tropical Pacific SSTs (e.g., all events of IPO+/La Niña minus La Niña) in order to quantitatively show and compare IPO's asymmetric modulation effect associated with a similar amount of IPO-related SST change. Because the largest circulation response for both ENSO and IPO appears during boreal winter

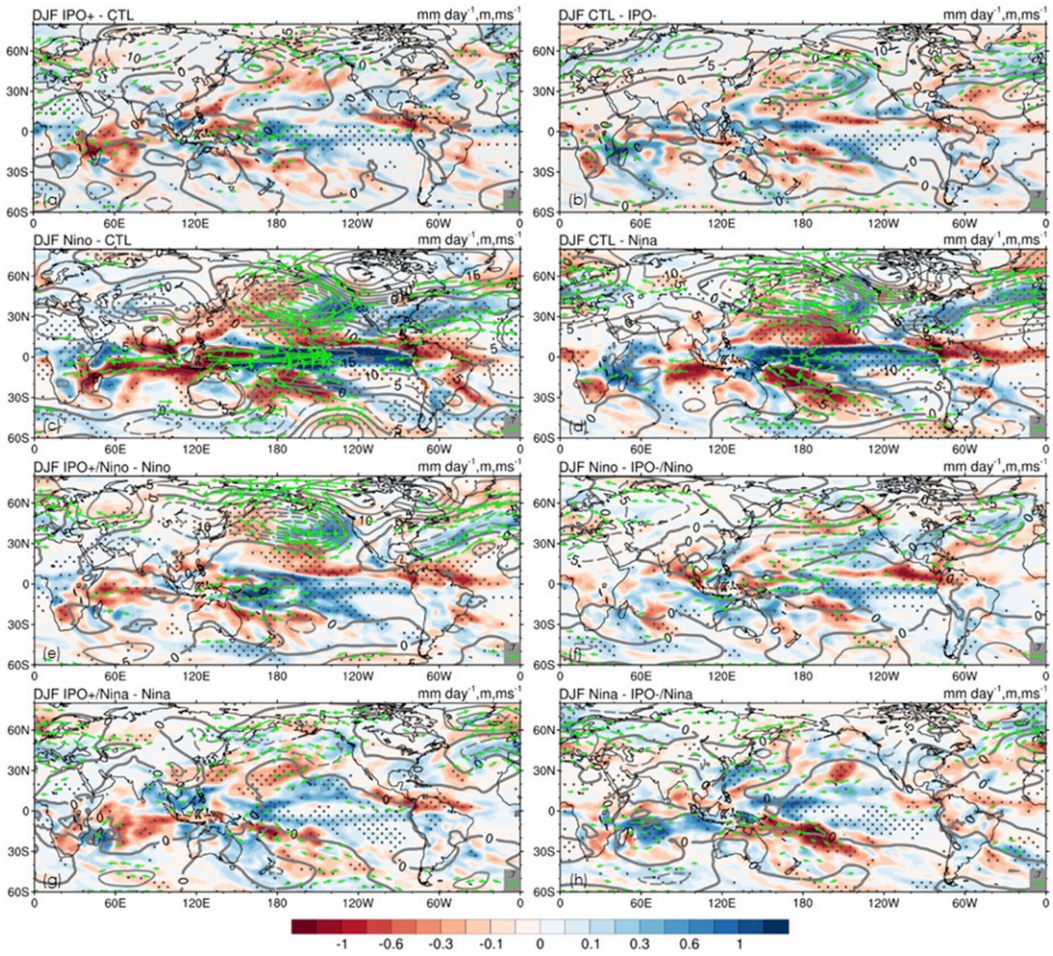

FIG. 13. As in Fig. 12, but for P (color shading; mm day^{-1}), geopotential height at 500 hPa (contours; m), and winds at 850 hPa (vectors; m s^{-1}).

(Figs. 2 and 3), here we only show composite maps for DJF.

Figure 8 shows that El Niño and La Niña's teleconnections are significantly modulated by the IPO, appearing as large increases in T over Alaska and western Canada, together with a deeper Aleutian low and stronger cyclonic winds for warm IPO phase. These net modulations seem to be stronger for IPO− (Figs. 8b,d) than IPO+ (Figs. 8a,c). Also, such patterns are more robust during El Niño (Figs. 8a,b) than during La Niña (Figs. 8c,d) and neutral ENSO (Figs. 8e,f). We found cold T anomalies over eastern Canada and Greenland for IPO+/El Niño (Fig. 8a) and IPO−/El Niño (Fig. 8b). They are similar to the spurious cooling pattern in Fig. 2g for IPO+, which suggests that the "AMO-like T influence" of the IPO largely arises from years when IPO is superimposed on El Niño. For the IPO+/La Niña (Fig. 8c), IPO−/La Niña, and IPO or neutral ENSO (Fig. 8d) cases, there are warm anomalies over northern China and Mongolia, which for the most parts are responsible for the eye-catching large Eurasia warming center shown for IPO+ (Fig. 2g). Furthermore, a unique change for the IPO+/La Niña case (Fig. 8c) is the warm anomaly over northeastern Australia, whereas such an IPO influence does not exist in El Niño boreal winters.

As P records over ocean (GPCP products) start from 1979, the sample sizes of the oceanic P composites are small. Hence, we primarily focus on P changes over land although the land P amplitudes are smaller than over the ocean. Over northeastern Australia, warm IPO-induced negative P anomalies are significant only during La Niña boreal winters (Figs. 9c,d), and this characteristic is largely responsible for the dry pattern over northeastern Australia during the IPO+ (Fig. 3g). In El Niño years (Figs. 9a,b), rainfall decreases significantly during IPO+, seen as a dry band across tropical Africa from 10°N to 20°S, Madagascar, and the western Indian Ocean. When La Niña takes places, warm IPO-induced

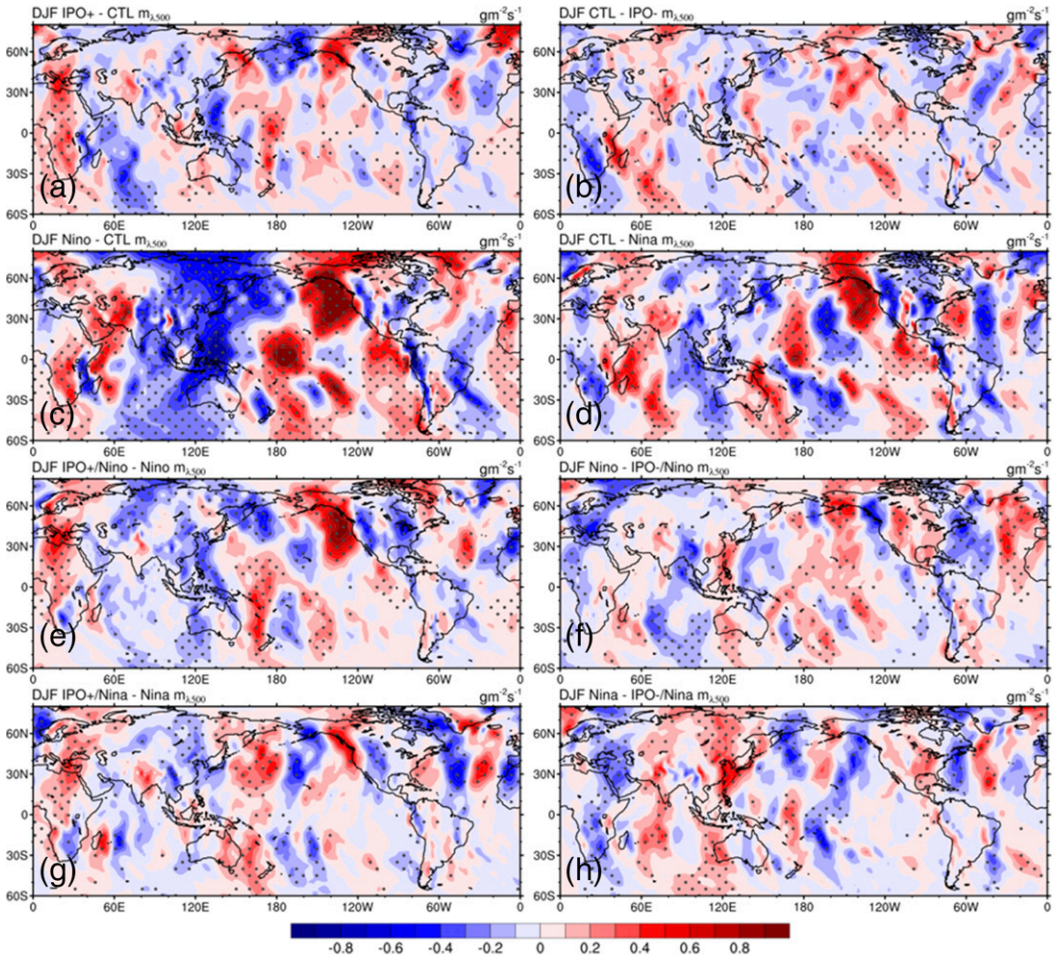

FIG. 14. As in Fig. 12, but for the 500-hPa m_λ (g m^{-2} s^{-1}).

negative P patterns are mostly confined to southern Africa, accompanied by wet anomalies along its east coast (Figs. 9c,d). During neutral ENSO years, the IPO's impacts on precipitation over land are mostly statistically insignificant. It shows, somehow, different results from Goodrich (2007), who showed that PDO has an impact on western United States winter precipitation during neutral ENSO years. One of the reasons is that we are investigating the IPO's net modulation effect within each ENSO category. Another possible reason is that the IPO index used in our study is uncorrelated with the ENSO index, in contrast to the PDO index, which still incorporates some high-frequency signal.

For the IPO's modulation of ENSO's influence on the EASM, we further show changes in P in the boreal summer following (JJA+) an ENSO winter (DJF) in Fig. 10. For boreal summers following a La Niña DJF, we found more significant "wet central China, dry north and south China" rainfall patterns during IPO+ than IPO− (Figs. 10c,d). Such a tripole P pattern also exists for El Niño (Figs. 10a,b) cases, but to a weaker degree. Circulation anomalies associated with these P changes are insignificant, possibly due to large sampling noise. Possible small sampling size–related precipitation changes are also seen in the tropical Pacific as insignificant and noisy anomaly patterns for IPO+/El Niño (Fig. 10a) and IPO+/La Niña (Fig. 10c).

In summary, the composite analyses show that IPO's modulation on ENSO teleconnections varies with both IPO and ENSO phases, although we have limited sampling because of the limited length of observations. To increase our confidence in these results, we performed a modeling investigation.

6. Model-simulated asymmetry of the IPO's modulation

The model results are shown only for DJF, when the atmospheric response is largest for all the perturbed-SST runs (Table 1). We use the difference between a

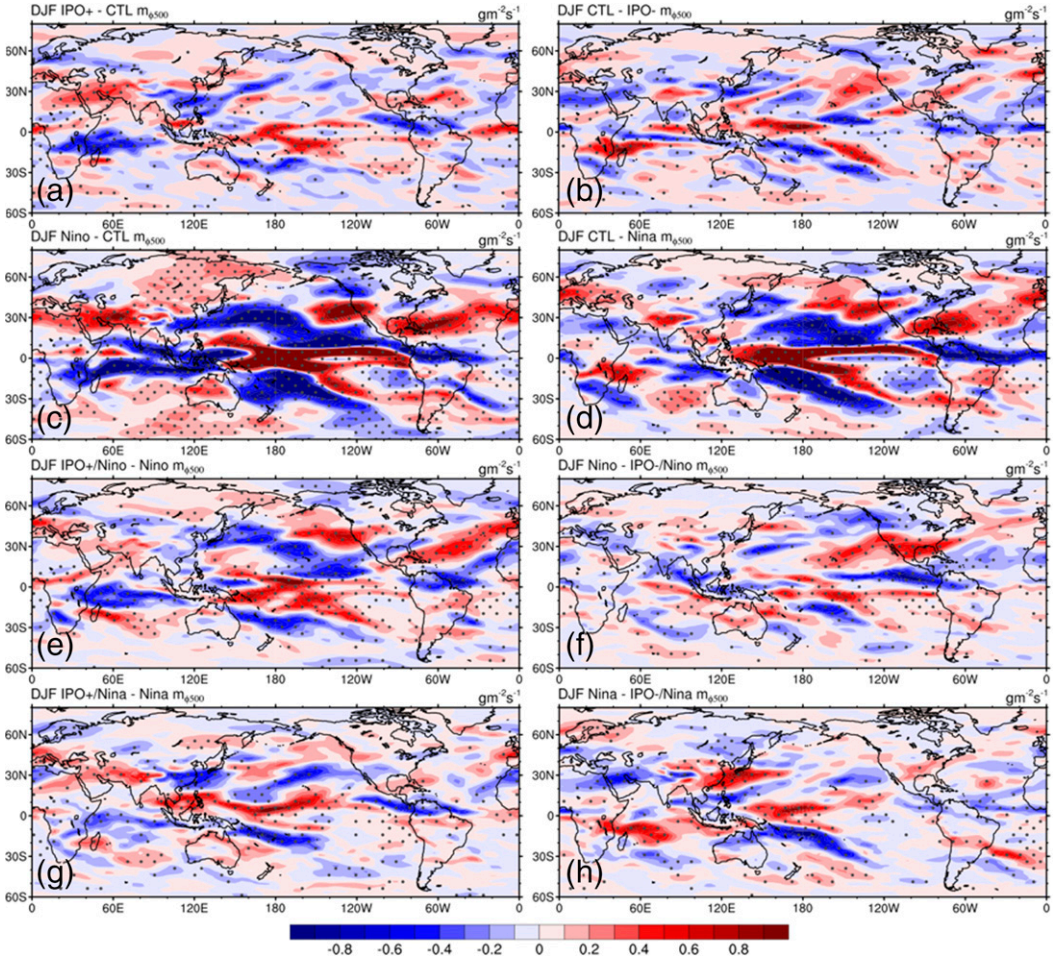

FIG. 15. As in Fig. 12, but for the 500-hPa m_ϕ ($g\,m^{-2}\,s^{-1}$).

combined IPO–ENSO SST case (Fig. 11) and its corresponding ENSO-only case (Figs. 12c–f, 13c–f, 14c–f, and 15c–f) to quantify IPO's modulation effect on ENSO's influence. We also show simulated El Niño's and La Niña's teleconnections maps (Figs. 12c,d, 13c,d, 14c,d, and 15c,d) and the IPO's direct influence (Figs. 12a,b, 13a,b, 14a,b, and 15a,b) from the ENSO-only or IPO-only cases (Table 1) as the reference for evaluating the modulation difference maps. These model-simulated ENSO and IPO teleconnection patterns may be compared with those discussed in section 4, while the modulation difference maps can be compared with those discussed in section 5. In general, the model-simulated DJF *T*, *P*, and circulation responses to the composite ENSO SST forcing alone broadly resemble those in observations or reanalyses (as shown by Figs. 2c and 12c, Figs. 3c and 13c, and Figs. A3 and A4 in the appendix), except the DJF *T* response to ENSO over the Arctic–northern Asia and Siberia. On the other hand, the model-simulated responses to the IPO SST forcing are generally weaker than and less consistent with observations, especially for *P* (as shown by Figs. 2g and 12a, Figs. 3g and 13a, and Figs. A5 and A6 in the appendix).

During neutral ENSO years, the IPO-related SST forcing produces insignificant *T* response over northern mid-to-high latitudes and other land areas, as Figs. 12a and 12b show opposite signs of *T* anomalies, even though Fig. 12b shows some *T* anomalies that are comparable to the observations (Fig. 8f). This may arise from the relatively weak IPO-related SST forcing (Figs. 11c,d) coupled with large internal variability at the northern latitudes (more discussion in section 7). However, when IPO+ is superimposed on El Niño, the IPO's modulation effect on *T* and atmospheric circulation (Fig. 12e) closely follows that from El Niño's impact (Fig. 12c) in a few regions such as the North Pacific and North America, where the simulated response roughly resembles that in observations (Fig. 8a). In contrast, a IPO− shows insignificant modulation of El Niño's influence on *T* over land such as Alaska and eastern Australia (Fig. 12f), although the

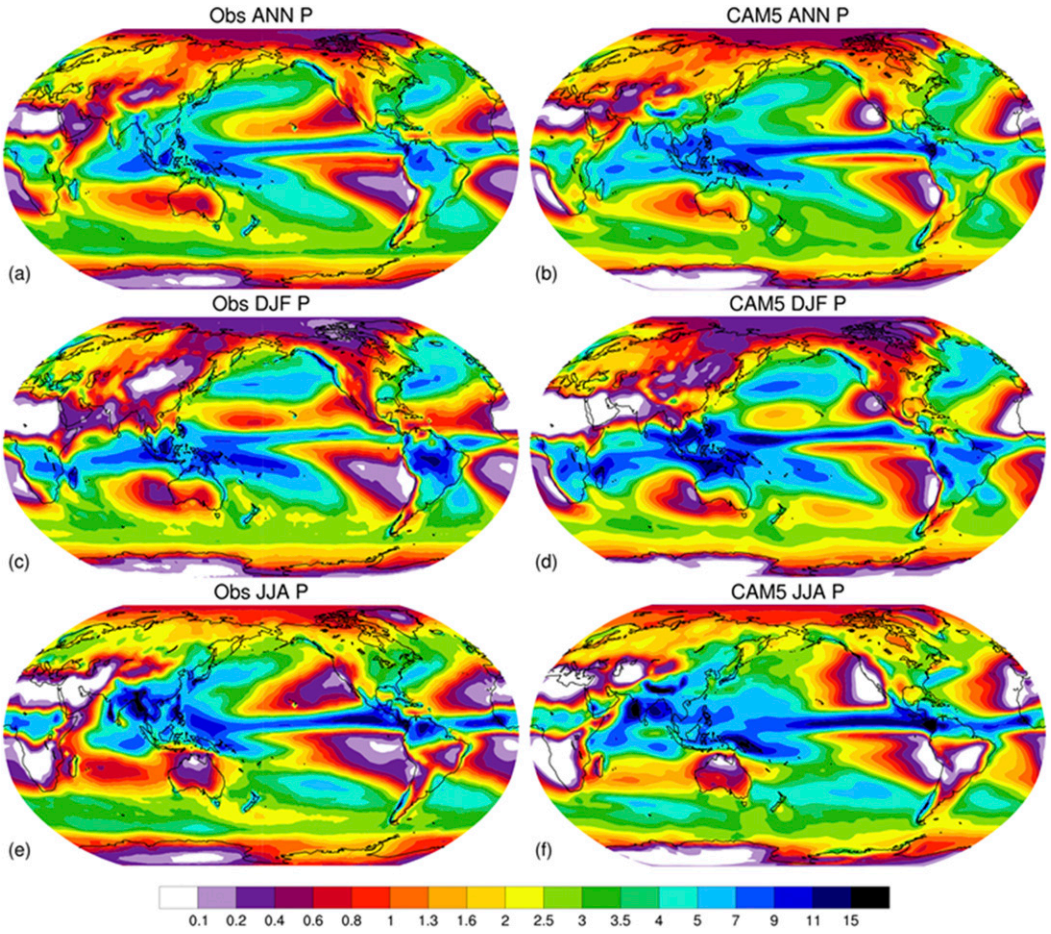

FIG. A1. Mean annual and seasonal precipitation (mm day^{-1}) from (a),(c),(e) observations and (b),(d),(f) CAM5 control run forced with climatological monthly SSTs. The observed precipitation is from the GPCC v7 dataset averaged over 1920–2014 for land and from GPCP v2.2 averaged over 1979–2014 over oceans.

modulation appears to be noticeable only over the northern latitudes in observations (Fig. 8b). Under La Niña conditions, unlike in observations (Figs. 8c,d), neither IPO+ nor IPO− induces significant and consistent modulation in T in the northern high latitudes, although the T anomalies over Alaska and Europe are fairly large but still statistically insignificant (Figs. 12g, h). This suggests a weak tropical–extratropical linkage with La Niña SST forcing in the CAM5 model. These results together imply an asymmetry in IPO's modulation of ENSO's influence on regional T. Specifically, the modulation varies nonlinearly with both ENSO and IPO phases: In the regions we focus on, El Niño–induced anomalies are enhanced by the warm IPO phase, but not weakened much by the cold IPO. In contrast, the La Niña–related T and wind anomalies are generally not significantly impacted by either IPO phase.

Figure 13 shows IPO's net modulation on ENSO-related P anomalies in the CAM5 experiments. The modulations on P over the tropical Pacific are well simulated in all perturbed cases as compared to observations in Fig. 9, with strengthened ITCZ and SPCZ. The dry rainfall band north of the ITCZ is also reasonably captured except during La Niña conditions (Figs. 9c,d and 13g,h). Precipitation over the Maritime Continent and western Indian Ocean does not show robust changes in simulations with La Niña conditions either (Figs. 13g,h). These patterns resemble, to a greater degree, El Niño (Figs. 3c and 13c) more than the warm phase of the IPO (Fig. 3g), which suggests that the IPO's modulation depends heavily on the background ENSO state. In the western tropical Indian Ocean, P decreases are found when IPO+ is superimposed on both El Niño and La Niña (Figs. 13e,g). The results suggest that the CAM5 is capable of reproducing the P response to the specified SST forcing over the Pacific.

Over land, we found robust patterns where P increases over southeastern South America and southwestern

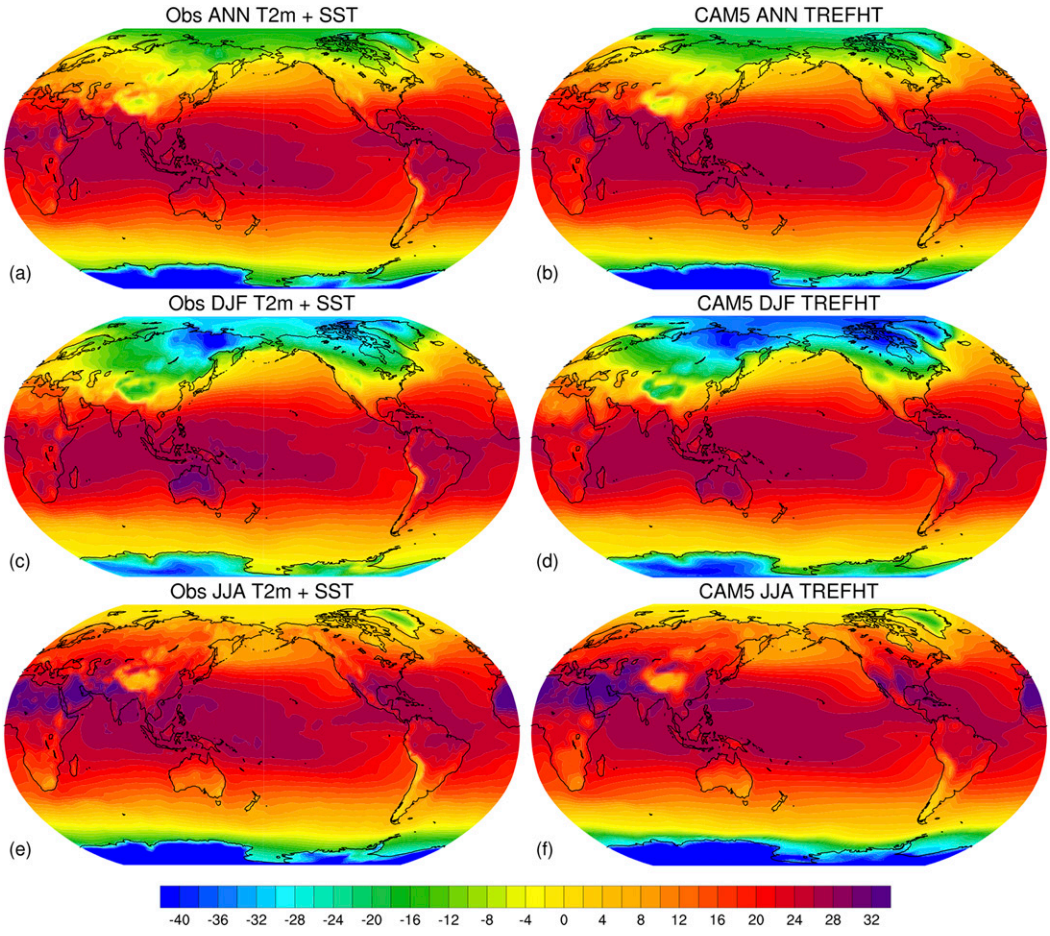

FIG. A2. As in Fig. A1, but for surface temperature (°C) averaged over 1920–2014 from the HadCRUT4 dataset (SST over oceans and surface air temperature over land) and the CAM5 control simulation (surface air temperature over the globe).

North America when either El Niño or La Niña occurs during IPO− (Figs. 13f,h). In southern Africa, significant drying is seen for IPO− and neutral ENSO (Fig. 13b), IPO+/El Niño (Fig. 13e), and IPO+/La Niña (Fig. 13g) cases, in contrast to our observational analyses, in which the southern African drying occurs only in IPO+/La Niña boreal winters (Fig. 9c). We do not see significant *P* modulations along the northeastern coastal region of Australia in any of the cases, mainly because ENSO-related *P* anomalies over Australia are not well simulated in CAM5 (Figs. 13c,d). Nevertheless, these modeling results indicate that, similar to the *T* modulations (Fig. 12), IPO's modulation on ENSO's influence on *P* depends on IPO phases. Specifically, for the regions where significant modulations are noted in CAM5, ENSO-related *P* anomalies are enhanced only by IPO−, except for southern Africa where ENSO's *P* anomaly is enhanced only by IPO+. The modulation also depends on ENSO phase and the modulation patterns primarily resemble ENSO teleconnections more than the IPO teleconnections.

Over tropical and subtropical land and oceans, rainfall changes closely follow changes in meridional overturning circulations (Fig. 14), as increases (decreases) in *P* concur with ascending (descending) motions. The relatively small changes in zonal overturning circulation (Fig. 15), however, do not seem to dominate rainfall changes. Specifically, modulation of the western branch of the Pacific Walker circulation is not well simulated in the experiments in comparison with the reanalysis (Fig. 4f), except for the IPO+/El Niño cases (Fig. 14e), which are responsible for the poorly simulated *P* anomalies along Australian east coast shown in Fig. 13.

7. Conclusions and discussion

We have investigated IPO's modulation effect on ENSO teleconnections using three different approaches,

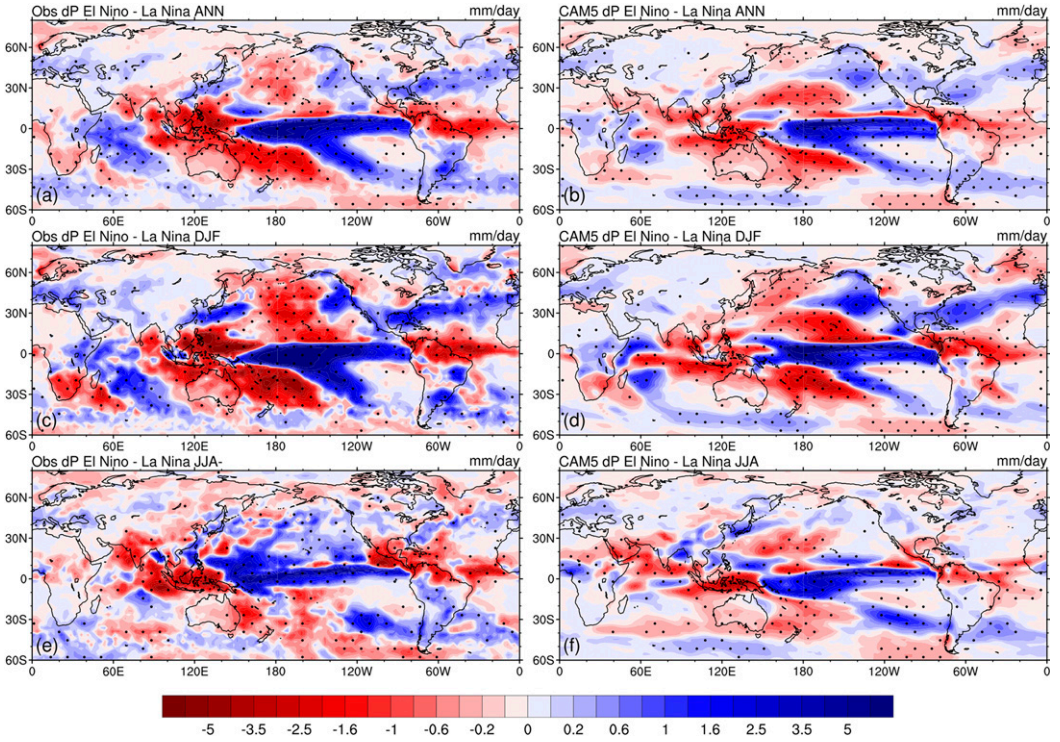

FIG. A3. Precipitation composite anomalies (mm day^{-1}) for El Niño minus La Niña years during 1920–2014 from (a),(c),(e) observations (oceans have data only for 1979–2014) and (b),(d),(f) the CAM5 simulations.

which include a linear regression and a composite analysis of long-term observational and reanalysis data, and atmospheric modeling experiments. Our study systematically compares the ENSO and IPO teleconnections in terms of their seasonality, magnitude, and spatial distribution. This presents a global picture of where, when, and how significant the IPO can modulate ENSO teleconnections. In contrast to previous studies that show varying ENSO teleconnections for different IPO phases, we have then explicitly quantified the net climatic influences of the IPO during different ENSO phases, which provides a clearer insight into the asymmetry of the modulation.

Observations and reanalyses show that while ENSO teleconnections are sustained over the course of the year and peak in boreal winter, the IPO-related T anomalies appear significant mainly in DJF and MAM. Spatially, ENSO's T teleconnections are widespread over the globe, while the IPO's T anomalies are most prominent and statistically significant over Eurasia, the North Pacific, and downstream in the western sector of North America. Significant T modulations appear over high-latitude land such as Alaska and western Canada, where the IPO-induced T anomalies are comparable to the ENSO-induced anomalies, although the IPO's SST forcing is much weaker. Responsible for such robust teleconnection is a prominent anomalous cyclone (anticyclone) over the North Pacific during El Niño and IPO+ (La Niña and IPO−), which emerged as an anomalous Aleutian low with varying strength during IPO and ENSO phases. It is essentially part of the PNA wave train that originates from tropical anomalous convection, as manifested in the 500-hPa height field. This result suggests that relatively small changes in tropical Pacific SSTs are largely responsible for the IPO's climate impacts in the extratropics. Despite our focus on DJF, it is worth noting that there is a southern counterpart of the PNA pattern, namely, the Pacific–South American (PSA) Rossby wave train (Mo and Higgins 1998; Mo and Paegle 2001), which manifests mostly in austral winter across from the tropical Indo-Pacific to South America.

The IPO-induced precipitation changes are noticeably smaller than those induced by ENSO, except for the changes during the summer monsoon in the Sahel and East Asia, where they are comparable in magnitude. In contrast to T teleconnections, P changes for both IPO and ENSO are attributable mainly to changes in meridional overturning circulation, with anomaly ascending (descending) mass fluxes linked to increases (decreases) in P, for instance, in the southwestern United States and the Maritime Continent. These circulation changes,

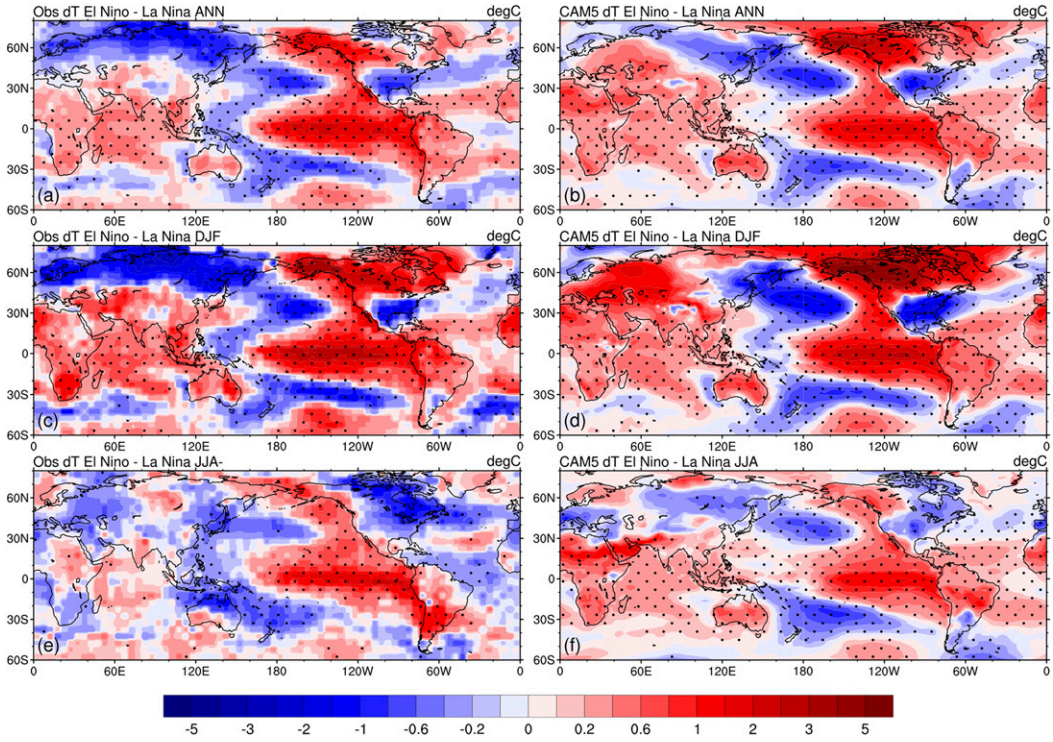

FIG. A4. As in Fig. A3, but for surface temperature anomalies (°C) (oceans have data for 1920–2014, and air temperatures over oceans in the model are largely determined by the specified SST forcing in the model runs).

which are closely linked to changes in tropical convection as a response to the ENSO and IPO SST forcing, are largely embedded in either the ascending or descending branches of the local Hadley circulation. This implies that the main cause for the IPO-induced rainfall anomalies originates from its anomalous tropical SSTs, although their magnitudes are small in comparison with the larger SST anomalies in the North Pacific. Changes in the local zonal overturning circulation (or local Walker circulation), on the other hand, explain a relatively small fraction of regional P anomalies, mainly for Australia. Similar to the T modulations, the same sign of ENSO's and IPO's P anomalies suggests that changes in P are amplified when the IPO and ENSO are in phase and dampened when they are out of phase.

Stratified by each of the ENSO and IPO phases, composite analyses of IPO's net modulation on ENSO teleconnections show that for a given ENSO state, modulations of IPO+ and IPO− on ENSO teleconnections are not identical in spatial distribution, and not symmetrically opposite in magnitude of T, P, and circulation anomalies, even if their SST anomalies are symmetrically opposite by definition. Also, the modulation depends not only on IPO phases but also on ENSO phases: teleconnections of a given IPO SST pattern differ substantially when the IPO is superimposed on El Niño, La Niña, or neutral ENSO state. While such asymmetry is noted mostly everywhere, one of the most prominent cases appears as IPO's T modulation in eastern Australia, where the modulation, shown as an enhanced warm anomaly, is significant only when IPO+ is superimposed on La Niña, but not for any other cases. However, because of the relatively small sampling size of observations, conclusions made from specific cases should be made with a high level of caution.

In theory, the asymmetry can be understood from the nonlinear Clausius–Clapeyron relation for saturation vapor pressure: for the same T departure, changes in atmospheric water vapor increase with the starting T when relative humidity does not change a lot. As such, during different ENSO phases, the same amount of IPO-induced SST change can trigger different responses in tropical convection. This notion also applies to the asymmetry of the modulation between IPO+ and IPO− for a given ENSO phase, as the atmospheric response to changes in T in opposite directions is not symmetrically opposite (i.e., a positive SST anomaly will induce a larger water vapor increase than the water vapor decrease induced by a negative SST anomaly of the same amount). In reality, however, the atmosphere responds to SST anomalies in a more complex way given that many feedbacks and stochastic perturbations are

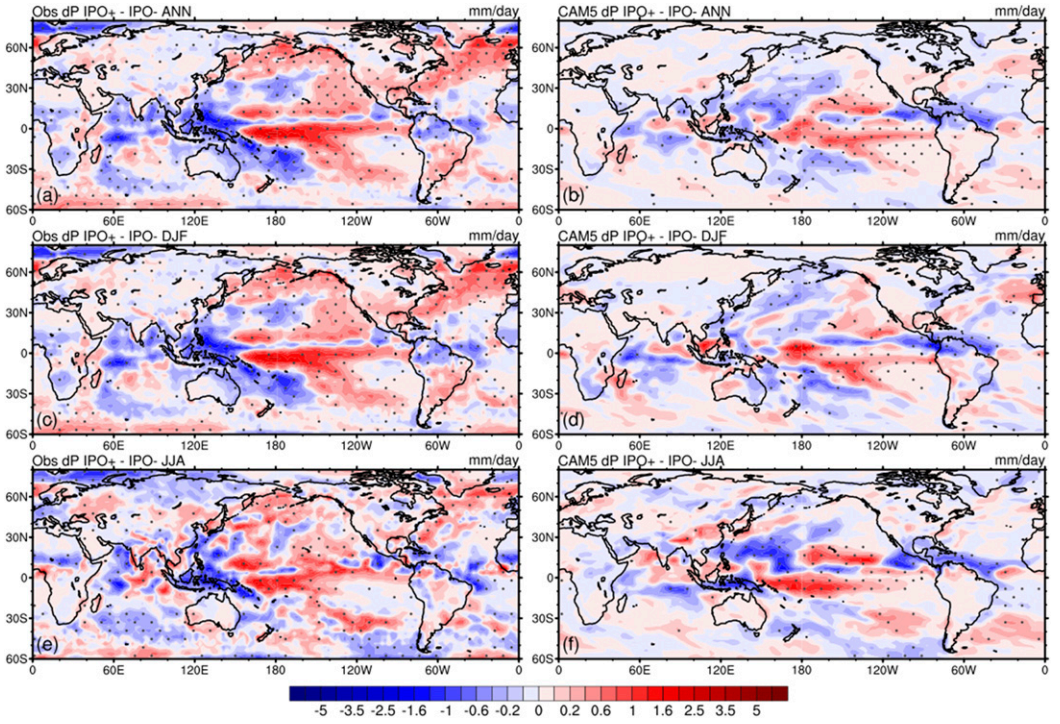

FIG. A5. Precipitation composite anomalies for IPO+ minus IPO− years during 1920–2014 from (a),(c),(e) observations and (b),(d),(f) the CAM5 IPO+ and IPO− experiments. The observed precipitation is from the GPCC v7 dataset over 1920–2014 for land and from the GPCP v2.2 over 1979–2014 over oceans.

involved, which can amplify or dampen the theoretically expected teleconnections. Also, because of the spatial heterogeneity of the IPO and ENSO SST patterns, teleconnections originating from a certain region can be affected by SST anomalies over other regions. As such, some of the asymmetric modulation shown in the composite maps (e.g., Siberian T anomaly) cannot be explained by the theoretical Clausius–Clapeyron relation with respect to SST anomalies over a specific region such as tropical or North Pacific, except those (e.g., western North American T and P anomalies and tropical Pacific P anomalies) closely linked to the strong tropical diabetic heating anomalies via either direct overturning circulation or Rossby wave trains.

The nonlinear modulation was examined in a series of CAM5 experiments forced with specified SSTs. Although the idealized experiments did not reproduce the IPO's modulations precisely everywhere, they do show that the modulation is unique for each ENSO–IPO combination, which echoes the asymmetry theory drawn from the composite analyses. The credibility of IPO modulation in the extratropical Northern Hemisphere largely depends on whether the CAM5 can realistically simulate the changes of the Aleutian low as part of the PNA-like Rossby wave train originating from the tropical Pacific. Such anomalous tropical–extratropical coupling depends heavily and asymmetrically on the background state of the tropical Pacific SSTs, as it is most evident during El Niño events but less clear during La Niña. This apparent asymmetry is consistent with the Clausius–Clapeyron relation: large anomalous convective heating and thus atmospheric teleconnections tend to occur when the tropical Pacific is in a warm state (i.e., El Niño) and the perturbation is toward a warm condition (i.e., IPO+). To a secondary degree, the extratropical anomalous atmospheric circulations are influenced also by the North Pacific SST anomalies. This notion is supported by the weaker and southward-displaced anomalous cyclonic flow over the North Pacific during the IPO−/El Niño case when compared with the IPO+/El Niño case.

We have conducted two additional simulations with doubled and tripled IPO+ SST anomalies, respectively. These SST configurations show large SST anomalies (up to 4.0°C) in the North Pacific while the SST changes in the tropical Pacific are still small (≤0.5°C). The absence of significant improvements for the teleconnections in these two experiments (not shown) supports our conclusion that depending on the ENSO state, IPO-induced additional changes in tropical Pacific SSTs dominate over changes in the North Pacific SSTs in triggering the IPO's modulations.

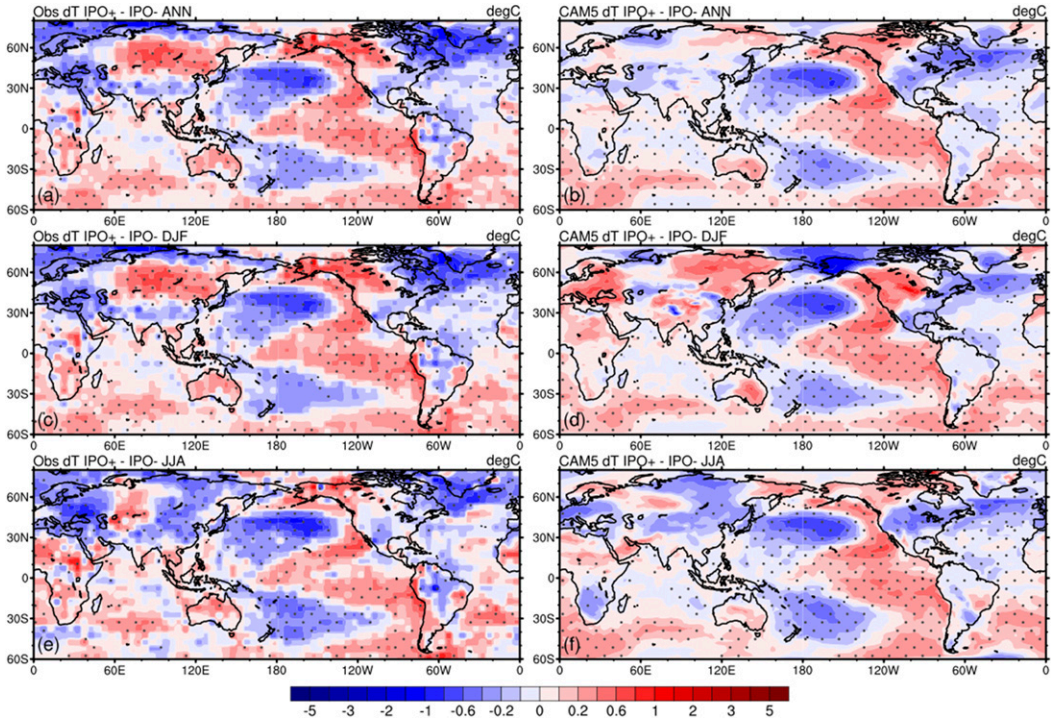

FIG. A6. As in Fig. A5, but for surface temperature anomalies. Observations are from the HadCRUT4 dataset over 1920–2014.

Ideally, a few more modeling experiments with separate tropical and extratropical SST anomalies could provide more insights into this concept. However, because of the main objective of this study and the limitation of computing resources, we leave these ideas to be tested in future work.

Our study further helps explain certain IPO modulation conundrums arising from some previous studies. For example, why does the running correlation between winter T over Alaska and western Canada and the Niño-3.4 SST index not vary with IPO phases (Dong and Dai 2015), when both IPO and ENSO have strong impacts over these regions? The reason seems to be that the IPO modulates T during all ENSO and IPO phases, according to our composite analyses. This aspect also applies to the southwestern United States where the ENSO–P running correlation does not vary with IPO phases (Dong and Dai 2015) because the IPO's modulation of ENSO's P anomaly is similar during both IPO+ and IPO−, a consequence of direct connection with anomalous local Hadley circulation. In Australia, the P versus Niño-3.4 SST running correlation does vary with IPO phases (Power et al. 1999; Dong and Dai 2015), which is mainly a result of the IPO's modulation of P during La Niña years. Indeed, the asymmetry may arise from the difference in the strength of IPO+ and IPO− defined by the IPO index. However, because of the limited length of observations in which there are only roughly two IPO cycles, we were unable to verify this hypothesis using observational data. Thus, caution should be exercised when interpreting the IPO's asymmetric teleconnections.

Acknowledgments. The authors thank Michael Reeder for his help on the local overturning circulation method in this study. We also thank the three anonymous reviewers for their constructive comments and suggestions. This work was supported by the U.S. National Science Foundation (Grants AGS-1353740 and OISE-1743738), the U.S. Department of Energy's Office of Science (Award DE-SC0012602), and the National Oceanic and Atmospheric Administration (Award NA15OAR4310086).

APPENDIX

CAM5 Model Evaluation

Evaluation of model simulated annual and seasonal T and P against observations. Comparisons are carried out for the long-term mean (Figs. A1 and A2), ENSO phases (Figs. A3 and A4), and IPO phases (Figs.A5 and A6).

REFERENCES

Alexander, M. A., K. Halimeda Kilbourne, and J. A. Nye, 2014: Climate variability during warm and cold phases of the Atlantic multidecadal oscillation (AMO) 1871–2008. *J. Mar. Syst.*, **133**, 14–26, https://doi.org/10.1016/j.jmarsys.2013.07.017.

Arblaster, J. M., G. A. Meehl, and A. M. Moore, 2002: Interdecadal modulation of Australian rainfall. *Climate Dyn.*, **18**, 519–531, https://doi.org/10.1007/s00382-001-0191-y.

Bice, D., A. Montanari, V. Vučetić, andM. Vučetić, 2012: The influence of regional and global climatic oscillations on Croatian climate. *Int. J. Climatol.*, **32**, 1537–1557, https://doi.org/10.1002/joc.2372.

Capotondi, A., and Coauthors, 2015: Understanding ENSO diversity. *Bull. Amer. Meteor. Soc.*, **96**, 921–938, https://doi.org/10.1175/BAMS-D-13-00117.1.

Chen, J. Y., A. D. Del Genio, B. E. Carlson, and M. G. Bosilovich, 2008: The spatiotemporal structure of twentieth-century climate variations in observations and reanalyses. Part II: Pacific pan-decadal variability. *J. Climate*, **21**, 2634–2650, https://doi.org/10.1175/2007JCLI2012.1.

Chen, W., J. Feng, and R. Wu, 2013: Roles of ENSO and PDO in the link of the East Asian winter monsoon to the following summer monsoon. *J. Climate*, **26**, 622–635, https://doi.org/10.1175/JCLI-D-12-00021.1.

Chung C. T. Y., S. B. Power, J. M. Arblaster, H. A. Rashid, and G. L. Roff, 2014: Nonlinear precipitation response to El Niño and global warming in the Indo-Pacific. *Climate Dyn.*, **42**, 1837–1856, https://doi.org/10.1007/s00382-013-1892-8.

Cohen, J., J. A. Screen, J. C. Furtado, M. Barlow, D. Whittleston, D. Coumou, and J. Jones, 2014: Recent Arctic amplification and extreme mid-latitude weather. *Nat. Geosci.*, **7**, 627–637, https://doi.org/10.1038/ngeo2234.

Compo, G. P., and Coauthors, 2011: The Twentieth Century Reanalysis Project. *Quart. J. Roy. Meteor. Soc.*, **137**, 1–28, https://doi.org/10.1002/qj.776.

Dai, A., 2013: The influence of the inter-decadal Pacific oscillation on US precipitation during 1923–2010. *Climate Dyn.*, **41**, 633–646, https://doi.org/10.1007/s00382-012-1446-5.

——, and T. M. L. Wigley, 2000: Global patterns of ENSO-induced precipitation. *Geophys. Res. Lett.*, **27**, 1283–1286, https://doi.org/10.1029/1999GL011140.

——, J. C. Fyfe, S.-P. Xie, and X. Dai, 2015: Decadal modulation of global surface temperature by internal climate variability. *Nat. Climate Change*, **5**, 555–559, https://doi.org/10.1038/nclimate2605.

da Silva, G. A. M., A. Drumond, and T. Ambrizzi, 2011: The impact of El Niño on South American summer climate during different phases of the Pacific decadal oscillation. *Theor. Appl. Climatol.*, **106**, 307–319, https://doi.org/10.1007/s00704-011-0427-7.

Deser, C., and M. L. Blackmon, 1993: Surface climate variations over the North Atlantic Ocean during winter: 1900–1989. *J. Climate*, **6**, 1743–1753, https://doi.org/10.1175/1520-0442(1993)006<1743:SCVOTN>2.0.CO;2.

——, A. S. Phillips, and J. W. Hurrell, 2004: Pacific interdecadal climate variability: Linkages between the tropics and the North Pacific during boreal winter since 1900. *J. Climate*, **17**, 3109–3124, https://doi.org/10.1175/1520-0442(2004)017<3109:PICVLB>2.0.CO;2.

Dong, B., and A. Dai, 2015: The influence of the interdecadal Pacific oscillation on temperature and precipitation over the globe. *Climate Dyn.*, **45**, 2667–2681, https://doi.org/10.1007/s00382-015-2500-x.

——, and ——, 2017: The uncertainties and causes of the recent changes in global evapotranspiration from 1982 to 2010. *Climate Dyn.*, **49**, 279–296, https://doi.org/10.1007/s00382-016-3342-x.

Dong, L., T. Zhou, A. Dai, F. Song, B. Wu, and X. Chen, 2016: The footprint of the inter-decadal Pacific oscillation in Indian Ocean sea surface temperatures. *Sci. Rep.*, **6**, 21251, https://doi.org/10.1038/srep21251.

Frauen, C., D. Dommenget, N. Tyrrell, M. Rezny, and S. Wales, 2014: Analysis of the nonlinearity of El Niño–Southern Oscillation teleconnections. *J. Climate*, **27**, 6225–6244, https://doi.org/10.1175/JCLI-D-13-00757.1.

Garreaud, R. D., M. Vuille, R. Compagnucci, and J. Marengo, 2009: Present-day South American climate. *Palaeogeogr. Palaeoclimatol. Palaeoecol.*, **281**, 180–195, https://doi.org/10.1016/j.palaeo.2007.10.032.

Gershunov, A., and T. P. Barnett, 1998: Interdecadal modulation of ENSO teleconnections. *Bull. Amer. Meteor. Soc.*, **79**, 2715–2725, https://doi.org/10.1175/1520-0477(1998)079<2715:IMOET>2.0.CO;2.

Goodrich, G. B., 2007: Influence of the Pacific decadal oscillation on winter precipitation and drought during years of neutral ENSO in the western United States. *Wea. Forecasting*, **22**, 116–124, https://doi.org/10.1175/WAF983.1.

——, and J. M. Walker, 2011: The influence of the PDO on winter precipitation during high- and low-index ENSO conditions in the eastern United States. *Phys. Geogr.*, **32**, 295–312, https://doi.org/10.2747/0272-3646.32.4.295.

Halpert, M. S., and C. F. Ropelewski, 1992: Surface temperature patterns associated with the Southern Oscillation. *J. Climate*, **5**, 577–593, https://doi.org/10.1175/1520-0442(1992)005<0577:STPAWT>2.0.CO;2.

Hartmann, B., and G. Wendler, 2005: The significance of the 1976 Pacific climate shift in the climatology of Alaska. *J. Climate*, **18**, 4824–4839, https://doi.org/10.1175/JCLI3532.1.

Hoerling, M. P., A. Kumar, and M. Zhong, 1997: El Niño, La Niña, and the nonlinearity of their teleconnections. *J. Climate*, **10**, 1769–1786, https://doi.org/10.1175/1520-0442(1997)010<1769:ENOLNA>2.0.CO;2.

Huffman, G. J., R. F. Adler, D. T. Bolvin, and G. Guojun, 2009: Improving the global precipitation record: GPCP version 2.1. *Geophys. Res. Lett.*, **36**, L17808, https://doi.org/10.1029/2009GL040000.

Hunke, E. C., W. H. Lipscomb, A. K. Turner, N. Jeffery, and S. Elliott, 2015: CICE: The Los Alamos Sea Ice Model documentation and software user's manual, version 5.1. Tech Doc. LA-CC-06-012, 116 pp., http://oceans11.lanl.gov/svn/CICE/tags/release-5.1.2/doc/cicedoc.pdf.

Hurrell, J. W., 1995: Decadal trends in the North Atlantic Oscillation: Regional temperatures and precipitation. *Science*, **269**, 676–679, https://doi.org/10.1126/science.269.5224.676.

——, and Coauthors, 2013: The Community Earth System Model: A framework for collaborative research. *Bull. Amer. Meteor. Soc.*, **94**, 1339–1360, https://doi.org/10.1175/BAMS-D-12-00121.1.

Krishnamurthy, L., and V. Krishnamurthy, 2014: Influence of PDO on South Asian summer monsoon and monsoon–ENSO relation. *Climate Dyn.*, **42**, 2397–2410, https://doi.org/10.1007/s00382-013-1856-z.

Krishnan, R., and M. Sugi, 2003: Pacific decadal oscillation and variability of the Indian summer monsoon rainfall. *Climate Dyn.*, **21**, 233–242, https://doi.org/10.1007/s00382-003-0330-8.

Kug, J.-S., F.-F. Jin, and S.-Il An, 2009: Two types of El Niño events: Cold tongue El Niño and warm pool El Niño. *J. Climate*, **22**, 1499–1515, https://doi.org/10.1175/2008JCLI2624.1.

Kwon, M., S.-W. Yeh, Y.-G. Park, and Y.-K. Lee, 2013: Changes in the linear relationship of ENSO–PDO under the global warming. *Int. J. Climatol.*, **33**, 1121–1128, https://doi.org/10.1002/joc.3497.

Larkin, N. K., and D. E. Harrison, 2005: Global seasonal temperature and precipitation anomalies during El Niño autumn and winter. *Geophys. Res. Lett.*, **32**, L16705, https://doi.org/10.1029/2005GL022860.

Li, J., R. Yu, W. Yuan, H. Chen, W. Sun, and Y. Zhang, 2015: Precipitation over East Asia simulated by NCAR CAM5 at different horizontal resolutions. *J. Adv. Model. Earth Syst.*, **7**, 774–790, https://doi.org/10.1002/2014MS000414.

Liu, Z. Y., 2012: Dynamics of interdecadal climate variability: A historical perspective. *J. Climate*, **25**, 1963–1995, https://doi.org/10.1175/2011JCLI3980.1.

López-Parages, J., B. Rodríguez-Fonseca, and L. Terray, 2015: A mechanism for the multidecadal modulation of ENSO teleconnection with Europe. *Climate Dyn.*, **45**, 867–880, https://doi.org/10.1007/s00382-014-2319-x.

Luo, D., Y. Xiao, Y. Yao, A. Dai, I. Simmonds, and C. L. E. Franzke, 2016a: Impact of Ural blocking on winter warm Arctic–cold Eurasian anomalies. Part I: Blocking-induced amplification. *J. Climate*, **29**, 3925–3947, https://doi.org/10.1175/JCLI-D-15-0611.1.

——, ——, Y. Diao, A. Dai, C. L. E. Franzke, and I. Simmonds, 2016b: Impact of Ural blocking on winter warm Arctic–cold Eurasian anomalies. Part II: The link to the North Atlantic Oscillation. *J. Climate*, **29**, 3949–3971, https://doi.org/10.1175/JCLI-D-15-0612.1.

——, Y. Yao, A. Dai, I. Simmonds, and L. Zhong, 2017a: Increased quasi stationarity and persistence of winter Ural blocking and Eurasian extreme cold events in response to Arctic warming. Part II: A theoretical explanation. *J. Climate*, **30**, 3569–3587, https://doi.org/10.1175/JCLI-D-16-0262.1.

——, Y. Chen, A. Dai, M. Mu, R. Zhang, and I. Simmonds, 2017b: Winter Eurasian cooling linked with the Atlantic multidecadal oscillation. *Environ. Res. Lett.*, **12**, 125002, https://doi.org/10.1088/1748-9326/aa8de8.

Mo, K. C., and R. W. Higgins, 1998: The Pacific–South American modes and tropical convection during the Southern Hemisphere winter. *Mon. Wea. Rev.*, **126**, 1581–1596, https://doi.org/10.1175/1520-0493(1998)126<1581:TPSAMA>2.0.CO;2.

——, and J. N. Paegle, 2001: The Pacific–South American modes and their downstream effects. *Int. J. Climatol.*, **21**, 1211–1229, https://doi.org/10.1002/joc.685.

Morice, C. P., J. J. Kennedy, N. A. Rayner, and P. D. Jones, 2012: Quantifying uncertainties in global and regional temperature change using an ensemble of observational estimates: The HadCRUT4 data set. *J. Geophys. Res.*, **117**, D08101, https://doi.org/10.1029/2011JD017187.

Neale, R. B., and Coauthors, 2010: Description of the NCAR Community Atmosphere Model (CAM 5.0). NCAR Tech. Note NCAR/TN-486+STR, 268 pp., http://www.cesm.ucar.edu/models/cesm1.1/cam/docs/description/cam5_desc.pdf.

Newman, M., and Coauthors, 2016: The Pacific decadal oscillation, revisited. *J. Climate*, **29**, 4399–4427, https://doi.org/10.1175/JCLI-D-15-0508.1.

Oleson, K. W., and Coauthors, 2013: Technical Description of version 4.5 of the Community Land Model (CLM). NCAR Tech. Note NCAR/TN-503+STR, 42o pp., https://doi.org/10.5065/D6RR1W7M.

Parker, D., C. Folland, A. Scaife, J. Knight, A. Colman, P. Baines, and B. Dong, 2007: Decadal to multidecadal variability and the climate change background. *J. Geophys. Res.*, **112**, D18115, https://doi.org/10.1029/2007JD008411.

Poli, P., and Coauthors, 2013: The data assimilation system and initial performance evaluation of the ECMWF pilot reanalysis of the 20th-century assimilating surface observations only (ERA-20C). ERA Rep. Series 14, 62 pp.

——, and Coauthors, 2016: ERA-20C: An atmospheric reanalysis of the twentieth century. *J. Climate*, **29**, 4083–4097, https://doi.org/10.1175/JCLI-D-15-0556.1.

Power, S., T. Casey, C. Folland, A. Colman, and V. Mehta, 1999: Inter-decadal modulation of the impact of ENSO on Australia. *Climate Dyn.*, **15**, 319–324, https://doi.org/10.1007/s003820050284.

Qian, Y., and Coauthors, 2015: Parametric sensitivity analysis of precipitation at global and local scales in the Community Atmosphere Model CAM5. *J. Adv. Model. Earth Syst.*, **7**, 382–411, https://doi.org/10.1002/2014MS000354.

Rayner, N. A., D. E. Parker, E. B. Horton, C. K. Folland, L. V Alexander, D. P. Rowell, E. C. Kent, and A. Kaplan, 2003: Global analyses of sea surface temperature, sea ice, and night marine air temperature since the late nineteenth century. *J. Geophys. Res.*, **108**, 4407, https://doi.org/10.1029/2002JD002670.

Ropelewski, C. F., and M. S. Halpert, 1987: Global and regional scale precipitation patterns associated with the El Niño/Southern Oscillation. *Mon. Wea. Rev.*, **115**, 1606–1626, https://doi.org/10.1175/1520-0493(1987)115<1606:GARSPP>2.0.CO;2.

Schneider, U., A. Becker, P. Finger, A. Meyer-Christoffer, M. Ziese, and B. Rudolf, 2014: GPCC's new land surface precipitation climatology based on quality-controlled in situ data and its role in quantifying the global water cycle. *Theor. Appl. Climatol.*, **115**, 15–40, https://doi.org/10.1007/s00704-013-0860-x.

Schwendike, J., P. Govekar, M. J. Reeder, R. Wardle, G. J. Berry, and C. Jakob, 2014: Local partitioning of the overturning circulation in the tropics and the connection to the Hadley and Walker circulations. *J. Geophys. Res. Atmos.*, **119**, 1322–1339, https://doi.org/10.1002/2013JD020742.

Trenberth, K. E., J. M. Caron, D. P. Stepaniak, and S. Worley, 2002: Evolution of El Niño–Southern Oscillation and global atmospheric surface temperatures. *J. Geophys. Res.*, **107**, 4065, https://doi.org/10.1029/2000JD000298.

Vertenstein, M., A. Bertini, T. Craig, J. Edwards, M. Levy, A. Mai, and J. Schollenberger, 2013: CESM user's guide (CESM1.2 release series user's guide). NCAR Tech. Note, 100 pp., http://www.cesm.ucar.edu/models/cesm1.2/cesm/doc/usersguide/ug.pdf.

Wallace, J. M., and D. S. Gutzler, 1981: Teleconnections in the geopotential height field during the Northern Hemisphere winter. *Mon. Wea. Rev.*, **109**, 784–812, https://doi.org/10.1175/1520-0493(1981)109<0784:TITGHF>2.0.CO;2.

Westra, S., B. Renard, and M. Thyer, 2015: The ENSO–precipitation teleconnection and its modulation by the interdecadal Pacific oscillation. *J. Climate*, **28**, 4753–4773, https://doi.org/10.1175/JCLI-D-14-00722.1.

Whitfield, P. H., R. D. Moore, S. W. Fleming, and A. Zawadzki, 2010: Pacific decadal oscillation and the hydroclimatology of western Canada—Review and prospects. *Can. Water Resour. J.*, **35**, 1–28, https://doi.org/10.4296/cwrj3501001.

Yuan, W., R. Yu, M. Zhang, W. Lin, J. Li, and Y. Fu, 2013: Diurnal cycle of summer precipitation over subtropical East Asia in CAM5. *J. Climate*, **26**, 3159–3172, https://doi.org/10.1175/JCLI-D-12-00119.1.

Zhang, Y., J. M. Wallace, and D. S. Battisti, 1997: ENSO-like interdecadal variability: 1900–93. *J. Climate*, **10**, 1004–1020, https://doi.org/10.1175/1520-0442(1997)010<1004:ELIV>2.0.CO;2.